TUDelft

Delft University of Technology

Ocean signatures in the total flux and polarization spectra of Earth-like exoplanets

Trees, V.J.H.; Stam, D.M.

Important note
To cite this publication, please use the final published version (if applicable).
Please check the document version above.

**Astronomy
&
Astrophysics**

Ocean signatures in the total flux and polarization spectra of Earth-like exoplanets[*]

V. J. H. Trees[1,2] and D. M. Stam[3]

[1] Royal Netherlands Meteorological Institute (KNMI), Utrechtseweg 297, 3731 GA, De Bilt, The Netherlands
e-mail: victor.trees@knmi.nl
[2] Faculty of Civil Engineering and Geosciences, Delft University of Technology, Stevinweg 1, 2628 CN Delft, The Netherlands
e-mail: v.j.h.trees@tudelft.nl
[3] Faculty of Aerospace Engineering, Delft University of Technology, Kluyverweg 1, 2629 HS Delft, The Netherlands

ABSTRACT

Context. Numerical simulations of starlight that is reflected by Earth-like exoplanets predict habitability signatures that can be searched for with future telescopes.
Aims. We explore signatures of water oceans in the flux and polarization spectra of this reflected light.
Methods. With an adding-doubling algorithm, we computed the total flux F, polarized flux Q, and degree of polarization P_s of starlight reflected by dry and ocean model planets with Earth-like atmospheres and patchy clouds. The oceans consist of Fresnel reflecting surfaces with wind-ruffled waves, foam, and wave shadows, above natural blue seawater. Our results are presented as functions of wavelength (from 300 to 2500 nm with 1 nm resolution) and as functions of the planetary phase angle from 90° to 170°.
Results. The ocean glint increases F, $|Q|$, and P_s with increasing phase angle at nonabsorbing wavelengths, and causes the spectra of F and $|Q|$ for the various phase angles to intersect. In the near-infrared, Q is negative, that is, the direction of polarization is perpendicular to the plane through the star, planet, and observer. In the P_s spectra, the glint leaves dips (instead of peaks) in gaseous absorption bands. All those signatures are missing in the spectra of dry planets.
Conclusions. The dips in P_s and the negative Q in the near-infrared can be searched for at a phase angle of 90°, where the planet-star separation is largest. Those ocean signatures in polarized light do not suffer from false positive glint signals that could be due to clouds or reflecting dry surfaces. For heavily cloudy planets, ocean detection is possible when the glint is (partially) cloud-free. When modeling signals of planets with oceans, using horizontally inhomogeneous cloud covers is thus crucial. Observations spread over time would increase the probability of catching a cloud-free glint and detecting an ocean.

Key words. radiative transfer – polarization – techniques: polarimetric – planets and satellites: oceans – techniques: spectroscopic – planets and satellites: terrestrial planets

1. Introduction

The discovery of liquid water on the surface of an extrasolar planet would be a milestone in the search for life beyond our Solar System, as liquid water is considered to be a requirement for life as we know it. Water oceans on the surfaces of rocky planets can be searched for in planetary systems' habitable zones, which are defined as the regions around stars where liquid surface water could be stable (Kasting et al. 1993). The actual capability of a planet to maintain liquid surface water is difficult to determine because that depends on, amongst others, the planet's atmospheric composition, as well as its vertical and horizontal pressure and temperature profiles, surface albedo, mass, size and rotational period, and the activity of its host star (see, e.g., Kopparapu et al. 2020).

Water vapor has already been detected in the atmospheres of hot gaseous extrasolar planets (e.g., Tinetti et al. 2007; Deming et al. 2013; Fraine et al. 2014; Kreidberg et al. 2014, 2015; Line et al. 2016) and of super Earth K2-18b which resides in the habitable zone of its parent star (Tsiaras et al. 2019). Those detections were done using spectroscopy of the transits of these

planets and/or of their secondary eclipses (when the planet moves behind the star). Although future transit or eclipse spectroscopy measurements of water vapor abundances on rocky planets, such as is planned with the *James Webb* Space Telescope (JWST), could give hints about habitable surface conditions, the light that is being detected with such measurements only traveled through the exoplanet's (upper) atmosphere, and actual observations of liquid water oceans are only possible using a direct detection of the starlight that is reflected by the planet.

The signal of starlight that is reflected by an Earth-like exoplanet and that reaches a (near-future) dedicated direct detection telescope does not provide any spatial resolution across an exoplanet, because of the enormous distances between the telescope and these planets. All information of the illuminated and visible part of the planetary disk is thus stored in one pixel. However, if the signal is measured at multiple wavelengths, the pixel contains information about, for example, the planet's color and absorbing gases. The signal also varies with the planetary phase angle (i.e., the angle between the observer, the host star and the planet orbiting its host star), as the optical properties of the surface and atmosphere usually depend on the scattering angle, and in time as the planet rotates around its axis.

Light from the star can be assumed to be unpolarized (Kemp et al. 1987), and it gets polarized upon scattering by the planet's

atmosphere and/or reflection by the surface. The state of polarization of the light thus enhances the contrast between the star and the exoplanet, but it also contains information about the optical properties of the planet's atmosphere and surface. The dependence of the degree of polarization on scattering angle is in general much more significant than that of the total flux (Hansen & Travis 1974), making polarimetry a strong tool for exoplanet characterization (see, e.g., Seager et al. 2000; Stam et al. 2004; Stam 2008). Indeed, also for detecting and characterizing oceans on exoplanets, the polarization of light provides an extra dimension. Fresnel reflection of direct starlight by an ocean results in a mirror reflection of the star in the water, which is called the glint, which broadens with increasing ocean surface roughness (i.e., wind speed). In the total reflected flux, the glint is strongest at the largest phase angles (see, e.g., Robinson et al. 2010, 2014), where unfortunately the separation between the planet and its star is relatively small and which is therefore not an optimal angle for resolving the planetary signal from the direct starlight. The degree of polarization, however, peaks at the Brewster angle, which is at larger and thus easier accessible planet-star separations (see Zugger et al. 2010; Trees & Stam 2019).

Measuring the degree of polarization also has practical advantages, because instrumental measurement errors in the total and polarized fluxes may cancel out upon division. Also, as a relative measure, the degree of polarization of an exoplanet is generally insensitive to extinction along the optical path between the exoplanet and the observer. That is, when taking measurements of an exoplanet in the night sky with a telescope on the Earth's surface, absorption of the light within the Earth's atmosphere affects the total and polarized fluxes equally, leaving the degree of polarization of the exoplanet unaffected.

Current ground-based and space-based telescopes are not capable of measuring the polarized light that is reflected by Earth-like exoplanets. Examples of instruments that are designed for measuring polarized light of exoplanets are EPOL (Keller et al. 2010), which is the imaging polarimeter of the Exoplanet Imaging Camera and Spectrograph (EPICS) for the European Southern Observatory's (ESO) Extremely Large Telescope (ELT) (Kasper et al. 2010), and POLLUX, a UV polarimeter that is envisioned for NASA's LUVOIR (Large UV Optical Infrared Surveyor) space telescope concept (Bouret et al. 2018). The choices in the design of those and other next generation instruments, their telescopes, and observational strategies (i.e., integration times and temporal coverage) depend on exoplanetary signals from numerical models.

Recently, numerical simulations of total flux spectra of Earth-like planets with rough ocean surfaces have been presented by Ryan & Robinson (2022), who suggested to retrieve the glint signal with a principal component analysis. Another suggested technique for ocean detection is to retrieve a surface type map from rotationally resolved phase curves of the total flux at a single or multiple wavelength(s) (Cowan et al. 2009; Oakley & Cash 2009; Lustig-Yaeger et al. 2018). None of the papers mentioned above studied the state of polarization of the reflected light. Without the polarization signal, false positive glint signatures may appear if in the crescent phase, reflecting surfaces or clouds have a relatively strong contribution. For example, Cowan et al. (2012) proposed that the larger coverage fraction of poles on the planetary disk in the crescent phase could mimic the glint.

Numerical simulations of starlight that is reflected by exoplanets with oceans that take polarization into account have first been presented by Stam (2008). Stam (2008) showed the spectra of the total flux and degree of polarization of Earth-like model exoplanets with oceans, vegetated surfaces and water clouds.

The ocean was described by a flat Fresnel reflecting surface on top of a black water body, without waves, wave shadows, foam, and reflecting water. Due to the flat ocean surface and the unidirectional incident sunlight, the glint was infinitely narrow and its signature was lost in the numerical integration over the planetary disk. Simulations of planets with rough black ocean surfaces as functions of planetary phase angle showed that the glint in fact gives a strong peak in the degree of polarization (see Williams & Gaidos 2008, who did not include the scattering by atmospheric gas). The glint shifts the peak of the degree of polarization at a phase angle of 90°, due to Rayleigh scattering by the gaseous molecules, to the Brewster angle at a larger phase angle (see Zugger et al. 2010, who included scattering by gas in the atmosphere). Zugger et al. (2011) proposed that for ocean detection absorption-free spectral windows in the infrared could be more convenient than visible wavelengths as there the scattering optical thickness of the atmosphere is smaller which improves the visibility of the glint.

The spectra of Stam (2008) and the phase curves of Zugger et al. (2011, 2010) are for horizontally homogeneous planets: the local atmosphere-surface systems do not vary in the latitudinal and longitudinal directions. The spectra of partly cloudy planets were mimicked by weighted sums of completely cloudy and completely cloud-free planets, which results in fading of the ocean signatures. Zugger et al. (2010, 2011) therefore concluded that the detectability of an exo-ocean is strongly limited by the presence of clouds. Trees & Stam (2019), however, simulated the total and polarized fluxes and the degree of polarization of light reflected by planets with rough ocean surfaces and with horizontally inhomogeneous clouds, and found that the glint appearing and hiding behind patchy clouds results in a variability of the phase curves. Moreover, Trees & Stam (2019) combined the phase curves at various wavelengths between 350 and 865 nm, to show that the glint increasingly reddens the degree of polarization and polarized flux with increasing phase angle. This color change in polarized light does not happen for dry planets and can thus identify an exo-ocean, also in the mean signal of heavily cloudy ocean planets with random patchy cloud patterns, and when surface pressures are higher than on Earth.

Modeled signals of Earth-like exoplanets can be validated with measurements of reflected sunlight by the Earth as a whole obtained from a sufficiently large distance. As far as we know, no such measurements of polarized light have yet been done, but an instrument that is in development to do so, is the Lunar Observatory of Unresolved Polarimetry of Earth (LOUPE; Klindžić et al. 2021; Hoeijmakers et al. 2016; Karalidi et al. 2012). Sunlight that is reflected by Earth can also be measured with an Earth-based telescope observing the night-side of the lunar disk in the sky, often referred to as Earth-shine measurements. Polarimetric Earth-shine measurements have been presented and analyzed by Bazzon et al. (2013), Miles-Páez et al. (2014), Sterzik et al. (2012, 2019, 2020) and Takahashi et al. (2013, 2021). The visible broadband measurements by Sterzik et al. (2019) indeed show a reddening of the degree of polarization with increasing phase angle, and Takahashi et al. (2021) found a shift of the peak degree of polarization toward phase angles larger than 90° in the near-infrared, which could be explained by the glint. It should be noted that, in Earth-shine measurements, the unknown, and depolarizing reflectance properties[1] of the lunar surface remain a considerable source of uncertainty.

---

[1] The Moon's reflectance properties of incident sunlight can rather straightforwardly be measured, but its reflectance properties of incident polarized light are unknown.

Attempts to fit model simulation results to measured Earth-shine spectra have been made by Emde et al. (2017). They used a model planet with a rough black ocean surface and patchy clouds at four wavelengths (469, 555, 645 and 858.5 nm), and concluded that the glint could explain the enhancement of the degree of polarization in the red part of the measured spectrum by Sterzik et al. (2012). Emde et al. (2017) also analyzed the influence of aerosols, water clouds and ice clouds on the degree of polarization spectra, but without an ocean below. We note that all spectra (i.e., at a 1 nm wavelength resolution) presented by Emde et al. (2017) were of (weighted sums) of horizontally homogeneous planets. Emde et al. (2017) did not show spectra of patchy cloudy planets with oceans, and did not study the phase angle variation of the spectropolarimetric glint signature.

In this paper, we present the computed spectra of the total and polarized fluxes and the degree of polarization of starlight that is reflected by dry and ocean planets, having Earth-like atmospheres with clouds consisting of spherical, liquid water droplets and horizontally inhomogeneous cloud patterns. Absorption of light in the planet's atmosphere by gaseous H_2O, O_2, O_3, CO_2 and CH_4 is taken into account. The wind over our oceans generates surface waves which broaden the ocean glint, wave shadows and sea foam, and the seawater has a natural blue color. The computed spectra range from the ultraviolet (300 nm) to the infrared (2500 nm) at a 1 nm wavelength resolution, and we present the results for planetary phase angles between 90° and 170°.

This paper is structured as follows. In Sect. 2, we state our definitions of the total and polarized fluxes and the degree of polarization of light. We explain our numerical method to compute those quantities for starlight reflected by our model planets, and we describe our atmosphere-ocean planet models. In Sect. 3, we present the computed spectra of the reflected total and polarized fluxes and the degree of polarization for dry and ocean planets. In Sect. 4, we discuss the influence of various atmospheric parameters on the ocean signature that we find in gaseous absorption bands in the degree of polarization. In Sect. 5, we compare our ocean signatures with earlier published results. Finally, in Sect. 6, we summarize the spectropolarimetric ocean signatures and state our conclusions.

2. Numerical method

2.1. Definitions of fluxes and polarization

The radiance and polarization state of a quasi-monochromatic light beam can be described by the following (column) vector $\boldsymbol{I}$

$$\boldsymbol{I} = [I, Q, U, V], \tag{1}$$

where I is the total radiance, Q and U the linearly polarized radiances, and V the circularly polarized radiance (see, e.g., Hansen & Travis 1974; Hovenier et al. 2004). The units of I, Q, U and V are W m^{-2} m^{-1} sr^{-1}, where m^{-1} indicates the dependence on wavelength λ and sr^{-1} are the units of solid angle Ω. In this paper, we also use the flux (column) vector $\pi\boldsymbol{F}$, described by

$$\pi\boldsymbol{F} = \pi[F, Q, U, V], \tag{2}$$

for which the units are W m^{-2} m^{-1}.

Elements Q and U are defined with respect to a reference plane. Because the distance between the observer and the exoplanet is much larger than the radius of the exoplanet, our reference plane is the planetary scattering plane, that is, the plane through the centers of the planet, the host star and the observer. The linearly polarized fluxes, πQ and πU, can then in principle

be obtained from the fluxes measured through a linear polarization filter perpendicular to the propagation direction of the light:

$$\pi Q = \pi F_{0°} - \pi F_{90°}, \tag{3}$$

$$\pi U = \pi F_{45°} - \pi F_{135°}, \tag{4}$$

where the subscripts indicate the rotation angles of the filter's optical axis with respect to the planetary scattering plane, measured in the anticlockwise direction when looking into the propagation direction of the light (see Hansen & Travis 1974; Hovenier et al. 2004). The total flux, πF, is measured according to

$$\pi F = \pi F_{0°} + \pi F_{90°} = \pi F_{45°} + \pi F_{135°}. \tag{5}$$

Elements Q and U can be converted to Q and U with respect to another reference plane, such as the optical plane of the polarimeter, using a rotation matrix (see Hovenier & van der Mee 1983).

We define the degree of polarization P, which is independent of the reference plane, as

$$P = \frac{\sqrt{Q^2 + U^2 + V^2}}{F}. \tag{6}$$

The starlight that is incident on a planet is assumed to be unpolarized ($P = 0$). This assumption is based on the very small degree of polarization of the disk-integrated sunlight (Kemp et al. 1987) (on the order of 10^{-6}) and of FGK-stars (Cotton et al. 2017) (23.0 ± 2.2 ppm for active stars and 2.9 ± 1.9 ppm for inactive stars), and on the small degree of polarization ($\sim 10^{-6}$) expected from stellar spots and flares breaking the symmetry of the stellar disk (Berdyugina et al. 2011; Kostogryz et al. 2015). We thus write the stellar flux vector that is incident on the exoplanet as $\pi\boldsymbol{F}_0 = \pi F_0 \boldsymbol{1}$ where $\boldsymbol{1}$ is the unit column vector and πF_0 is the incident stellar flux measured perpendicular to the direction of propagation.

With unpolarized incident starlight and if the planet is mirror-symmetric with respect to the reference plane, the integrated πU and πV over the planetary disk will equal zero. In this paper, all cloud-free and fully cloudy planets are mirror-symmetric while the planets with patchy clouds are near mirror-symmetric with respect to the planetary scattering plane resulting in πU and πV being a factor 10^3 and 10^5, respectively, smaller than πF. Therefore, we may use an alternative definition of the degree of polarization, namely

$$P_s = -\frac{Q}{F} = -\frac{F_{0°} - F_{90°}}{F_{0°} + F_{90°}}. \tag{7}$$

For $P_s > 0$ ($P_s < 0$), the light is polarized perpendicular (parallel) to the reference plane.

2.2. Computing the reflected starlight

Starlight with wavelength λ that is reflected by an orbiting planet arrives at an observer at a large distance from the planet-star system. Consider a point O on the planet's surface (see Fig. 1) at latitude δ and longitude ϑ which are defined with respect to the vector from the planet's center toward the observer. If stellar flux πF_0 is incident at O, the reflected intensity vector toward
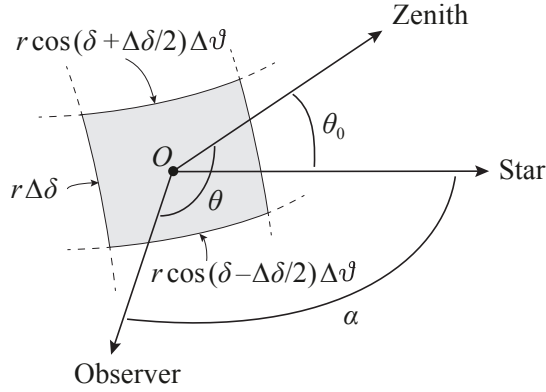
Fig. 1. Sketch of the geometry of the reflection at location O on the exoplanet, with latitude δ and longitude ϑ. Quantities r, θ, θ_0 and α are the planetary radius, viewing zenith angle, stellar zenith angle, and planetary phase angle, respectively. The gray area element represents the area on the planet subtended by latitude element $\Delta\delta$ and longitude element $\Delta\vartheta$.
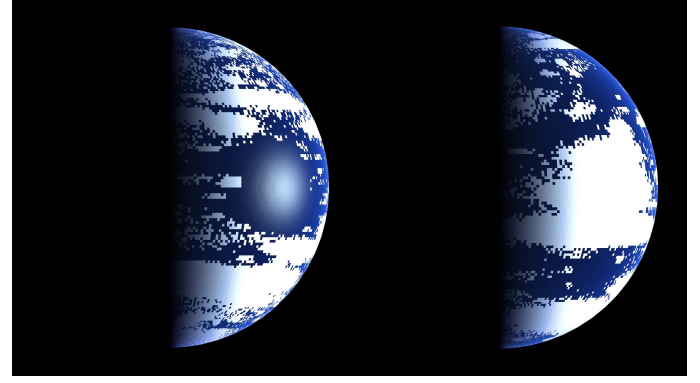

Fig. 2. Disk-resolved computed RGB images using weighted additive color mixing of the pixel intensity $\overline{F}_{ij}\pi r^2/(\mu_{ij}\Delta O_{ij})$ at $\lambda = 450$, 550, and 650 nm, at $\alpha = 90°$ of ocean planets with patchy clouds and a cloud-free glint (*left image*) and a cloud-covered glint (*right image*). For both images, the cloud fraction f_c equals 0.5, and the surface wind speed v is $7\,\text{m s}^{-1}$.

the observer can be written as (see Stam et al. 2006; Hansen & Travis 1974):

$$\mathbf{I}(\lambda, \mu, \mu_0, \phi - \phi_0) = \mu_0\, \mathbf{L}(\beta)\, \mathbf{R}(\lambda, \mu, \mu_0, \phi - \phi_0)\mathbf{1}\, F_0(\lambda), \qquad (8)$$

where $\mu_0 = \cos\theta_0$ with $0° \leq \theta_0 \leq 90°$ the local stellar zenith angle, $\mu = \cos\theta$ with $0° \leq \theta \leq 90°$ the local viewing zenith angle, and $\phi - \phi_0$ the azimuth difference angle between the incident and reflected beam ($\phi - \phi_0 = 0°$ when the propagation directions of the incident and reflected beams are in the same vertical half plane). Furthermore, $\mathbf{R}$ is the 4×4 reflection matrix of the atmosphere-surface system at O. Since the optical properties of the atmosphere and surface are wavelength dependent, $\mathbf{R}$ also depends on wavelength. The 4×4 rotation matrix $\mathbf{L}(\beta)$ converts Q and U that are defined with respect to the local meridian plane (through the local zenith and the direction to the observer) directly after the reflection at O, to Q and U defined with respect to the planetary scattering plane (see Hovenier & van der Mee 1983). Angle β is the rotation angle between the two reference planes, which is positive in the anticlockwise direction when looking in the direction of light propagation. Quantities μ, μ_0, $\phi - \phi_0$ and β depend on location (δ, ϑ). Quantities μ_0 and $\phi - \phi_0$ also depend on the phase angle α, which is the angle between the star and the observer measured from the planet's center (at $\alpha = 0°$, the planet is behind the star as seen from the observer, and at $\alpha = 180°$, the planet is precisely in front of the star). We set the orbital plane equal to the planetary scattering plane (i.e., the orbit is seen "edge-on"), and the tilt of the planet's rotation axis with respect to the orbital plane's normal is set equal to zero.

The reflected flux vector by the planet as a whole, arriving at the observer at a distance d from the planet can be obtained for each λ and α by integrating $\mathbf{I}$ over the solid angle subtended by the planetary disk (see, e.g., Stam et al. 2006):

$$\pi\mathbf{F}(\lambda, \alpha) = \frac{1}{d^2} \int_{\mathbb{D}} \mu\, \mathbf{I}(\lambda, \mu, \mu_0, \phi - \phi_0)\, dO. \qquad (9)$$

We normalize $\pi\mathbf{F}$, indicated by $\overline{\mathbf{F}}$, such that at $\alpha = 0°$, its first element $\overline{F}$ equals the planet's geometric albedo as follows

$$\overline{\mathbf{F}}(\lambda, \alpha) = \frac{\pi\mathbf{F}(\lambda, \alpha)}{\pi F_0(\lambda)} \frac{d^2}{r^2}. \qquad (10)$$

Here, r is the radius of the planet. We compute $\overline{\mathbf{F}}$ independent of πF_0, r and d. By specifying those parameters for a given exoplanet-star system, the values of $\overline{\mathbf{F}}$ presented in this paper can straightforwardly be converted to $\pi\mathbf{F}$ of the given system using Eq. (10). The degree of polarization P (or P_s) is independent of πF_0, r and d.

To evaluate Eq. (9), we divide the planet's surface into elements ΔO_{ij} centered at points O_{ij} located at (δ_i, ϑ_j), with angular dimensions $\Delta\delta$ and $\Delta\vartheta$ such that

$$\Delta O_{ij} = \int_{\vartheta_j - \Delta\vartheta/2}^{\vartheta_j + \Delta\vartheta/2} \int_{\delta_i - \Delta\delta/2}^{\delta_i + \Delta\delta/2} r^2 \cos\delta\, d\delta\, d\vartheta$$
$$= 2r^2\Delta\vartheta \cos\delta_i \sin(\Delta\delta/2). \qquad (11)$$

Combining Eqs. (8)–(10), and replacing the integral in Eq. (9) by a summation, we arrive at

$$\overline{\mathbf{F}}(\lambda, \alpha) \approx \sum_{j=1}^{M} \sum_{i=1}^{N} \mu_{0ij}\, \mathbf{L}(\beta_{ij})\mathbf{R}_{ij}(\lambda, \mu_{ij}, \mu_{0ij}, \phi_{ij} - \phi_{0ij})\mathbf{1}\, \frac{\mu_{ij}\Delta O_{ij}}{\pi r^2}, \qquad (12)$$

where N and M are the number of latitudes and longitudes, respectively. At locations that are out of view ($\theta_{ij} > 90°$) or not illuminated ($\theta_{0ij} > 90°$), $\mathbf{R}_{ij} = 0$. The projections of ΔO_{ij} on a plane perpendicular to the observer's viewing direction are approximately $\mu_{ij}\Delta O_{ij}$. Hence, the integration error at $\alpha = 0°$ can be expressed by the deviation of $\sum_{j=1}^{M} \sum_{i=1}^{N} \mu_{ij}\Delta O_{ij}/(\pi r^2)$ from 1. We use $\Delta\delta = \Delta\vartheta = 1°$, resulting in an integration error at $\alpha = 0°$ of about 2×10^{-15}.

The computation of $\overline{\mathbf{F}}$ is performed at wavelengths λ from 300 to 2500 nm with a step size of 1 nm. To compute $\overline{\mathbf{F}}$ for a given phase angle α and locations (δ_i, ϑ_j), we first compute ΔO_{ij}, μ_{ij}, μ_{0ij}, $\phi_{ij} - \phi_{0ij}$ and β_{ij}, and we select a local atmosphere-surface model for each location. We precompute $\mathbf{R}$ of the local atmosphere-surface models (see Sect. 2.3) for each λ on a grid of 100 μ-points, 100-μ_0 points and a Fourier-series representation for the azimuth direction (see de Haan et al. 1987; Rossi et al. 2018, for details about the Fourier series expansion). We interpolate between those grids to obtain $\mathbf{R}_{ij}$ at (δ_i, ϑ_j) and λ for locally reflected light in the direction of the observer, and evaluate Eq. (12).
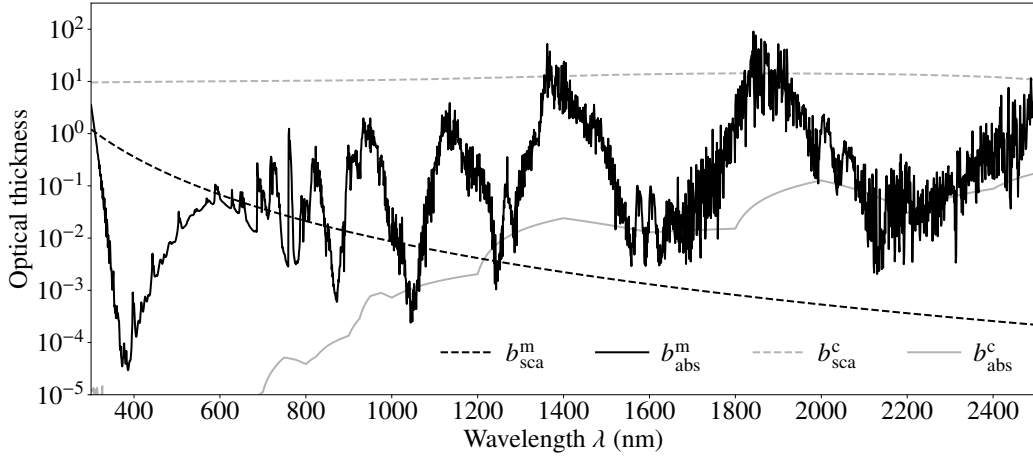
Fig. 3. Optical thickness of the model atmosphere for scattering by gas b_{sca}^m (black dashed line), absorption by gas b_{abs}^m (black solid line, see Fig. 4 for the values per gas species), scattering by water cloud droplets b_{sca}^c (gray dashed line) and absorption by water cloud droplets b_{abs}^c (gray solid line).
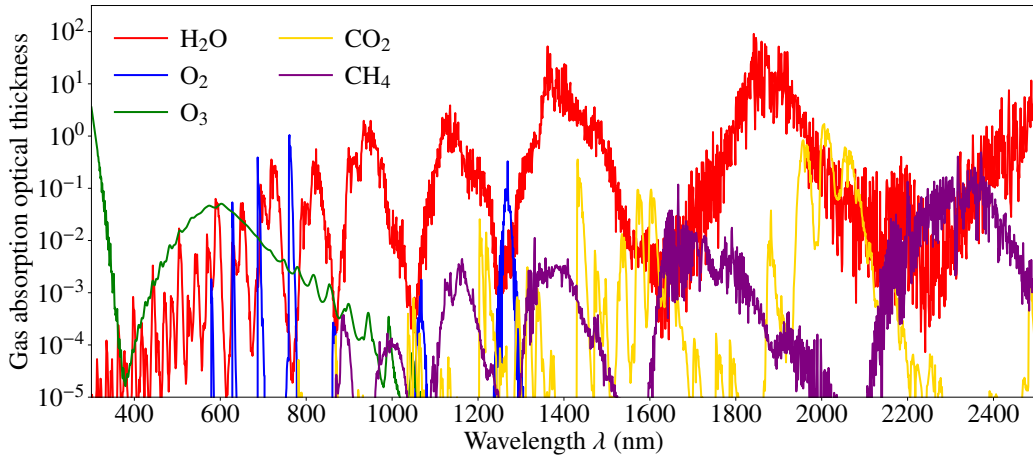

Fig. 4. Absorption optical thicknesses of the various gases in our model atmosphere, computed by taking the natural logarithm of the 1 nm bin averaged direct line-by-line transmittance of each absorbing gas (see, e.g., Eq. (1) of Irwin et al. 2008). In our computations, we do not use these values directly, instead we use 10 k-distribution Gauss points in each 1 nm wide wavelength bin (see the text for more details).

For our horizontally homogeneous planets the precomputed **R** can be used for each location on the planet. For our horizontally inhomogeneous planets, that is, our planets that have cloudy and cloud-free locations, one **R** is precomputed for the cloudy areas and another one for the cloud-free areas. We generate the patchy cloud locations randomly on the planet for each α and in a zonally oriented pattern. Figure 2 shows two RGB images of our ocean planet models with horizontally inhomogeneous cloud patterns at $\alpha = 90°$. The cloud fraction f_c on the visible and illuminated part of the planetary disk is 0.5 in both images, but in the image on the left the ocean glint is cloud-free while it is fully covered by clouds on the right.

2.3. The planetary surface–atmosphere models

The local reflection matrix **R** (Eq. (12)) depends on the optical properties of the local atmosphere and surface. It is computed with a multistream adding-doubling radiative transfer algorithm taking into account polarization of light for all orders of scattering (see de Haan et al. 1987; Stam 2008), extended with reflection by and transmission through a rough ocean surface and scattering in the water body (see Trees & Stam 2019). Below, we describe our atmosphere and surface models.

2.3.1. The atmosphere

The atmospheres of our local atmosphere-surface models consist of a stack of 16 horizontally homogeneous layers. For each layer, the optical thickness b, the single-scattering albedo a and the scattering matrix $\mathbf{F}_{sca}$ (see Hovenier et al. 2004) of the mixture of molecules and cloud particles need to be specified to perform the radiative transfer calculations. We refer to Stam (2008) and the references therein for the relevant equations. We use cloud-free atmospheres, in which light is scattered and absorbed only by gaseous molecules, and cloudy atmospheres, that also have cloud particles that scatter and absorb light.

In our model atmospheres, gas molecules scatter as anisotropic Rayleigh scatterers (see Hansen & Travis 1974), with the wavelength-dependent depolarization factor of Bates (1984) between 300 and 1000 nm which we extrapolate to 2500 nm, the refractive index of dry air varies with wavelength (Peck & Reeder 1972) and the mean molecular mass is 29 g mole^{-1}. The acceleration of gravity is 9.81 m s^{-2}. The molecular density in a layer depends on the pressure difference across each layer. We use the pressure-temperature profile throughout the 16 layers as specified in Table 1 of Stam (2008), which is based on the mid-latitude summer profile of McClatchey et al. (1972).

Our mix of atmospheric gases is Earth-like. It consists of ozone (O_3), water vapor (H_2O), oxygen (O_2), methane (CH_4), and carbon dioxide (CO_2). The volume mixing ratios (VMRs) of O_3 and H_2O in each layer are taken from Table 1 of Stam (2008). The VMRs of O_2, CH_4 and CO_2 are assumed constant with height: 0.21, 1.7×10^{-6} and 410×10^{-6}, respectively. The molecular absorption cross sections of O_3 are from Gorshelev et al. (2014) and Serdyuchenko et al. (2014), and depend on the layer's temperature. The molecular absorption cross sections of O_2, H_2O, CH_4, and CO_2 are from the HITRAN database (Gordon et al. 2017) with the HAPI package (Kochanov et al. 2016), and depend on the pressure and temperature of the layer.

Figures 3 and 4 show the optical thickness of the model atmosphere for molecular scattering (b_{sca}^m) and molecular absorption (b_{abs}^m) ranging from 300 to 2500 nm at a 1 nm wavelength resolution. The value of b_{sca}^m decreases with increasing wavelength according to the λ^{-4}-dependence of the Rayleigh scattering cross section. The value of b_{abs}^m varies strongly with λ in Fig. 3, but also within the 1-nm wide bins. Therefore, we do not use b_{abs}^m directly but convert the molecular absorption cross sections of the gas mixture to so-called k-distributions (Lacis & Oinas 1991; Stam et al. 2000), using 10 Gaussian quadrature points per wavelength bin. The absorbing molecules responsible for enhanced values of b_{abs}^m in Fig. 3 can be identified using Fig. 4. It should be noted that while the concentrations of CH_4, O_2 and CO_2 are assumed to be altitude independent, H_2O mainly resides and thus absorbs in the bottom layers of our model atmosphere while O_3 mainly resides and thus absorbs in the top layers (see Table 1 of Stam 2008).

In a cloudy atmosphere, the clouds also contribute to the scattering and absorption optical thicknesses, the single-scattering albedo, and the scattering matrix (see Stam 2008). For consistence with Stam (2008), we assume spherical homogeneous water cloud droplets with a standard size distribution (Hansen & Travis 1974), having an effective radius of 2.0 μm and an effective variance of 0.1. The cloud base altitude is 2 km ($p = 802$ hPa) and the cloud top altitude is 4 km ($p = 628$ hPa). The cloud droplet single scattering albedo, scattering matrix and wavelength dependence of the droplet extinction cross section are computed using Mie-theory (De Rooij & van der Stap 1984). The real and imaginary parts of the refractive index of the water droplets vary with wavelength between 300 and 2500 nm from $1.3490 + (1.60 \times 10^{-8})i$ to $1.2605 + (2.06 \times 10^{-3})i$ (Hale & Querry 1973). The cloud optical thickness b^c is 10 at $\lambda = 550$ nm, and varies with wavelength between 300 and 2500 nm from 9.57 to 11.01 (and peaks with 14.35 at 1887 nm) according to the wavelength dependence of the droplets' extinction cross–section. The cloud droplets absorb radiation in the infrared too, although their scattering contribution is much larger at all wavelengths as can be seen in Figs. 3 and 4.

Figure 5 shows the phase functions and the degree of linear polarization P_s of unpolarized incident light that is singly scattered by the gaseous molecules and the cloud droplets. From this figure it is clear that the single scattering properties of the cloud droplets depend on wavelength across the entire range between 300 and 2500 nm. For example, the diffraction peak in the phase function near $\Theta = 0°$ weakens with increasing λ. Also, the sign changes of P_s depend on λ and the secondary rainbow feature, which is near $\Theta = 120°$ for $\lambda = 300$ nm, is unobservable for $\lambda \gtrsim 1000$ nm. The phase function and P_s of the gaseous molecules also depend on λ according to the wavelength dependence of the depolarization factor of air, but as can be seen in Fig. 5, this dependence is very small.

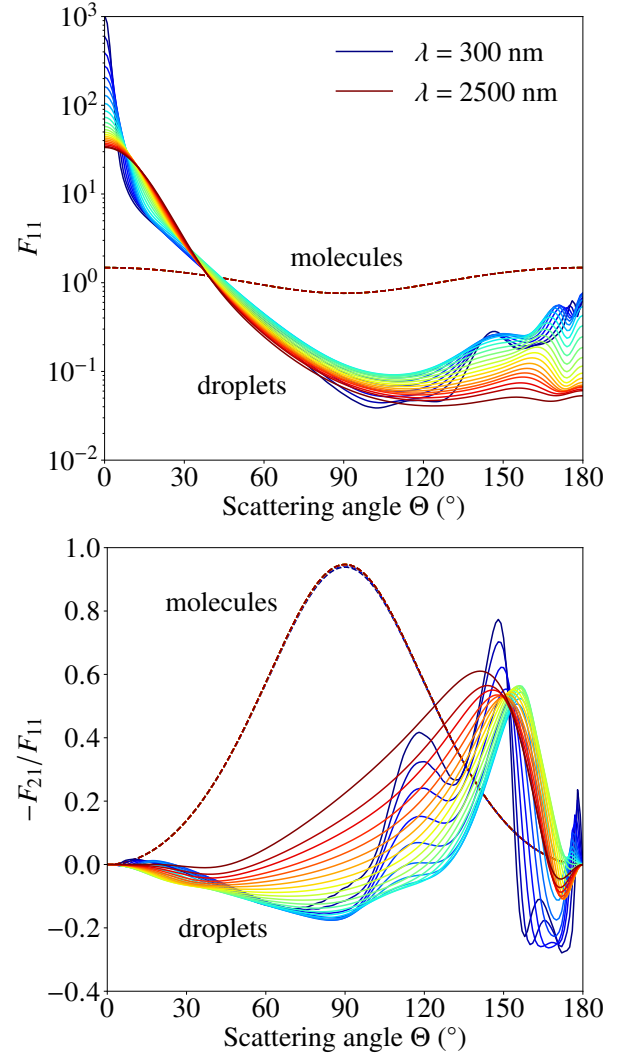**Fig. 5.** Phase function F_{11} (element (1,1) of scattering matrix $\boldsymbol{F}_{sca}$) (*top*) and degree of linear polarization ($-F_{21}/F_{11}$) (*bottom*) as functions of the scattering angle Θ, for singly scattered light by gaseous molecules (dashed lines) and cloud droplets (solid lines). Scattering angle Θ is the angle between the directions of propagation of the incident and the scattered light ($\Theta = 180° - \alpha$). The wavelengths range from 300 nm (dark blue line) to 2500 nm (dark red line), in steps of 100 nm. The lines for the gaseous molecules at the different wavelengths virtually overlap.

2.3.2. The surface

Below the atmosphere, the surface of our model planets is either a Lambertian reflector (i.e., isotropically reflecting and completely depolarizing), or an ocean. The ocean consists of a Fresnel reflecting and transmitting air-water interface, a water body below the interface and a surface below the water body (see Appendix A of Trees & Stam 2019, for the relevant equations). Other than in Stam (2008), where the Fresnel reflecting ocean is flat, our ocean surface can be rough as it can be ruffled by the wind. The Fresnel reflection by the air-water interface of incident starlight that is directly transmitted through the exoplanet's atmosphere results in the so–called ocean glint, whose size depends on the surface roughness. The surface roughness depends on the wind speed according to the empirical relation between wind speed and wave slope inclination distribution of Cox & Munk (1954). The width of the glint pattern increases with increasing
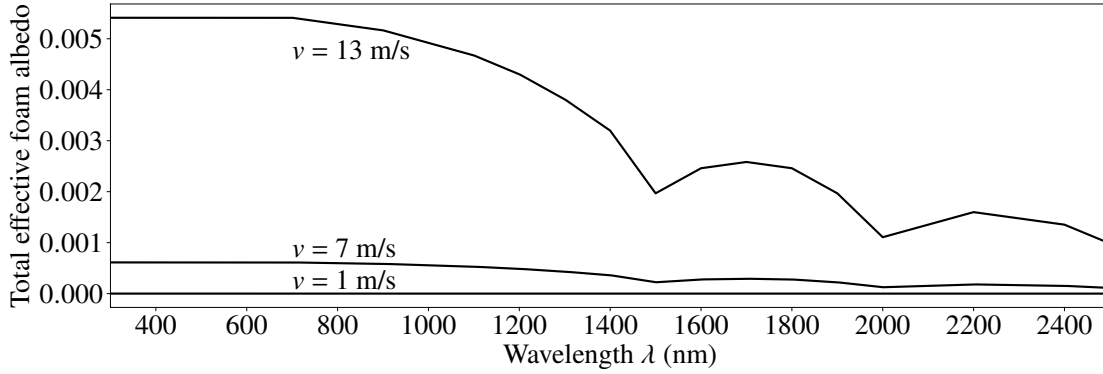
Fig. 6. Total effective sea foam albedo, which is the effective foam albedo of Koepke (1984) taking into account the aging of the whitecaps on the seawater multiplied by the wind-speed dependent fraction of the ocean surface that is covered with whitecaps of Monahan & Muircheartaigh (1980): $2.95 \times 10^{-6} v^{3.52}$, with v the wind speed in m s^{-1}.
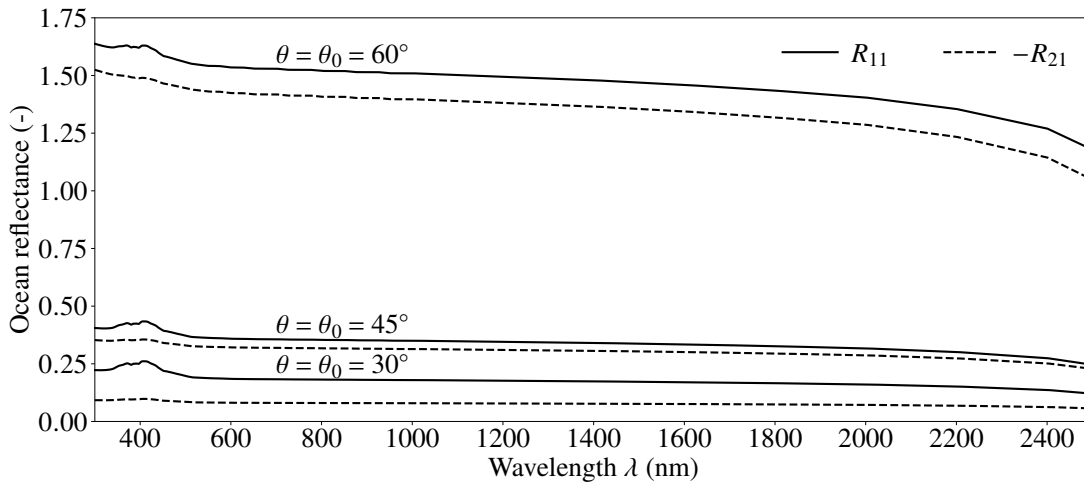

Fig. 7. Reflectance of the model ocean from 300 to 2500 nm for $\phi - \phi_0 = 0°$ and $\theta = \theta_0 = 30°$, 45° and 60°. R_{11} is the total reflectance (element (1,1) of matrix $\mathbf{R}_{\text{ocean}}$), and $-R_{21}$ is the linearly polarized reflectance (element (2,1) of $\mathbf{R}_{\text{ocean}}$). The wind speed v is 7 m s^{-1}.

wind speed, while its brightness gradually decreases (see Fig. 7 of Trees & Stam 2019). We use wind speeds of 1 m s^{-1} (light breeze), 7 m s^{-1} (moderate breeze), and 13 m s^{-1} (strong breeze).

With increasing wind speed the contribution of sea foam in our ocean model also increases (according to Monahan & Muircheartaigh 1980). We assume that the foam reflects Lambertian (isotropic and depolarizing). Although the foam albedo is approximately constant across the visible (~0.22), for wavelengths longer than 1000 nm, the albedo decreases significantly, see Fig. 6. Therefore we use the effective wavelength-dependent albedo of Koepke (1984) that decreases from 0.22 to 0.04 between 300 and 2500 nm. This albedo takes into account the aging of the whitecaps on the waves. The net contribution of the foam to the total ocean reflectance across our wavelength range is shown in Fig. 6. In the following, we call this contribution the "total effective foam albedo". For $v = 13$ m s^{-1}, 2.45% of the ocean surface is covered with foam, while for $v = 7$ m s^{-1} and $v = 1$ m s^{-1}, it is 0.28% and 2.96 $\times 10^{-4}$%, respectively, which explains the strong dependence of the total effective foam albedo on v (see also Eq. (A.15) of Trees & Stam 2019). With increasing wind speed, the influence of wave shadows (i.e., the blockage of incident and/or reflected light by waves) also increases, which is taken into account using the shadowing function of Smith (1967) and Sancer (1969). The reflection and transmission matrices of the air-water interface are corrected for the energy deficiency

caused by neglecting reflections of light between different wave facets (Nakajima 1983).

Light that is transmitted through the air-water interface is scattered and/or absorbed by the water or absorbed by the surface below the water body. For consistence with Trees & Stam (2019), we assume a 100 m deep ocean and a black surface. The water body is modeled as a stack of horizontally homogeneous layers of pure seawater, and its reflectance is computed using an adding-doubling program taking into account multiple scattering, absorption and polarization (de Haan et al. 1987). The single scattering properties of the seawater are approximated by the scattering matrix for anisotropic Rayleigh scattering (Hansen & Travis 1974) with a depolarization factor of 0.09 (Chowdhary et al. 2006; Morel 1974). The absorption and scattering coefficients are taken from Sogandares & Fry (1997), Pope & Fry (1997) and Smith & Baker (1981), resulting in a blue color across the visible. For wavelengths longer than 800 nm, all radiation that is transmitted through the air-water interface is absorbed by the water. For more details on our ocean model, we refer to Trees & Stam (2019).

The Fresnel reflection (and transmission) by (and through) the air-water interface depends on the real refractive index of water (see Appendix A of Trees & Stam 2019). The real refractive index of air is set equal to 1.0 in the interface computations of our ocean model. The real refractive index of water

(Hale & Querry 1973) is approximately constant across the visible (it varies from 1.339 at 400 nm to 1.330 at 750 nm), but decreases more significantly in the near-infrared to 1.2605 at 2500 nm (see also Sect. 2.3.1). Therefore, unlike in the ocean model of Trees & Stam (2019), we use the wavelength-dependent water refractive index of Hale & Querry (1973) when computing the reflection and transmission matrices of the air-water interface (Eqs. (A.1) and (A.6) of Trees & Stam 2019).

Figure 7 shows elements (1,1) and (2,1) of $\mathbf{R}_{ocean}$, the reflection matrix of the ocean (thus without the atmosphere), from 300 to 2500 nm, for three geometries in the forward reflection direction. These elements represent the total and the linearly polarized reflectances of the ocean, respectively. For a nonisotropic reflecting surface, such as a Fresnel reflecting surface, the reflectance can be larger than 1.0 because it is directional (for an isotropically reflecting surface, such as a Lambertian reflecting surface, the reflectance is equal to the surface albedo and thus always smaller than or equal to 1.0). With increasing θ and θ_0, the reflection angle at the air-water interface increases and the Fresnel reflection strengthens, resulting in a larger reflectance, that is, a brighter glint. The spectral signature of the ocean glint is relatively flat: there is only a slight decrease with wavelength, except for $\lambda \lesssim 400$ nm and $\lambda \gtrsim 2000$ nm where the spectral slopes are steeper as a result of the wavelength dependence of the water refractive index. The bump in the visible, between 300 and 500 nm, is responsible for the blue color of the seawater.

Figure 7 also shows the linearly polarized reflectance of the ocean. The spectral shape of this reflectance follows the spectral shape of the total reflectance. The degree of polarization increases with increasing θ and θ_0 from 30° to 45°, because the number of randomly oriented wave facets that experience local incidence angles equal or close to the Brewster angle (which is 53° in the visible) increases[2]. For θ and θ_0 larger than 53°, the degree of polarization decreases again, but the absolute linearly polarized reflectance increases as the total ocean reflectance strengthens (as shown by the spectrum for $\theta = \theta_0 = 60°$). The linearly polarized ocean reflectance between 300 and 500 nm slightly increases because of the higher ocean reflectance and because the light that leaves the water gets partly polarized upon scattering inside the water.

As explained in Trees & Stam (2019), our energy balance, reflection and transmission matrices for the rough air-water interface have been verified against Nakajima (1983), Mishchenko & Travis (1997) and Zhai et al. (2010). More recently, Chowdhary et al. (2020) published results for the (polarized) reflectance by locally plane-parallel atmosphere-ocean models, as a benchmark for state-of-the-art spectropolarimetric radiative transfer models, as a preparation for NASA's upcoming Plankton, Aerosol, Cloud, ocean Ecosystem (PACE) Earth observation satellite mission (Chowdhary et al. 2019; Werdell et al. 2019). We compared against Chowdhary et al. (2020), for the rough ocean model without atmosphere (their model AOS-2) and with molecular atmosphere (their model AOS-3). The absolute differences of R_{11} and $|R_{21}|$ with respect to those of Chowdhary et al. (2020) were smaller than 3.7×10^{-4} for all scattering geometries of the test results, and were on average of the order 10^{-5}.

3. Results

Here, we present the computed spectra of the total flux $\overline{F}$ (Sect. 3.1) and polarized flux $\overline{Q}$ (Sect. 3.2), normalized using

---

[2]   At the Brewster angle, the degree of polarization of light reflected by a clean and flat air-water interface reaches its maximum of 1.0.
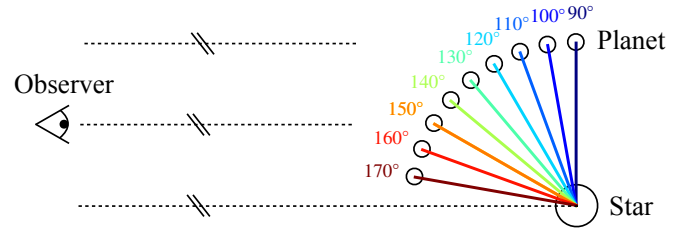
Fig. 8. Sketch of the observing geometries used in our computations, for various phase angles α. The α-dependent colors correspond to the colors of the α-dependent spectra in Figs. 9–14, 17 and 18.

the geometric albedo as explained in Sect. 2.2, and the degree of polarization P_s (Sect. 3.3) of starlight that is reflected by our model planets.

3.1. Total flux $\overline{F}$

3.1.1. $\overline{F}$ of cloud-free planets

Figure 9a shows the computed total flux $\overline{F}$ that is reflected by cloud-free model planets with dry, Lambertian reflecting surfaces, for λ between 300 and 2500 nm and at nine phase angles α from 90° to 170° (see Fig. 8). The surface albedo a_s increases in the subfigures from top to bottom: $a_s = 0.0$, 0.1 and 0.8.

The $\overline{F}$ spectra at $\alpha = 90°$ that are presented in Fig. 9a, agree well with published model computations between 300 and 1000 nm by Stam (2008): for planets with dark surfaces ($a_s = 0.0$ and 0.1) and for $\lambda > 340$ nm, $\overline{F}$ decreases with increasing λ because of the λ^{-4} dependence of the Rayleigh scattering efficiency by the gas. With increasing a_s, $\overline{F}$ increases at all λ outside the absorption bands because of the contribution of light that is reflected by the surface. With increasing α, $\overline{F}$ decreases at all λ outside the absorption bands for all surface albedos. This decrease of $\overline{F}$ for larger α is a direct consequence of the smaller illuminated and visible fraction of the planetary disk (see, e.g., Fig. 4 of Stam 2008, for the planetary phase curves of $\overline{F}$ for dry planets with various surface albedos).

Superimposed on the continua of the surface reflectance and the scattering gas, are gaseous absorption features (cf. the gaseous absorption optical thicknesses in Fig. 4). For example, O_3 absorbs the reflected light in the so-called Huggins absorption band at $\lambda < 340$ nm, and in the so-called Chappuis absorption band between 500 and 700 nm. The absorption in the Chappuis band is more apparent when the surface albedo is higher (see the results for $a_s = 0.8$). For $a_s = 0.1$ and 0.8, the O_2-A band (around $\lambda \sim 760$ nm) can clearly be identified, whereas the other O_2 absorption bands are more easily confused with H_2O absorption bands (cf. Fig. 4). For a more detailed discussion of the absorption features in the $\overline{F}$ spectra of Earth-like planets between 300 and 1000 nm, see, for example, Sect. 4.1.1 of Stam (2008).

Here, we extend the spectra toward the near-infrared (NIR): from 1000 to 2500 nm. In this spectral range, the main gaseous absorber is H_2O, with absorption bands near 1150, 1400, 1900, and 2500 nm (cf. Fig. 4). It should be noted that O_2 has an absorption band at about 1270 nm, thus well-separated from H_2O absorption bands, which can also be identified in Fig. 9a. This O_2 absorption feature has already been observed in measured disk-integrated IR $\overline{F}$ spectra of the Earth during the EPOXI mission (see Livengood et al. 2011; Fujii et al. 2013). Small absorption features of CO_2 near 1600 nm can also be identified. Absorption
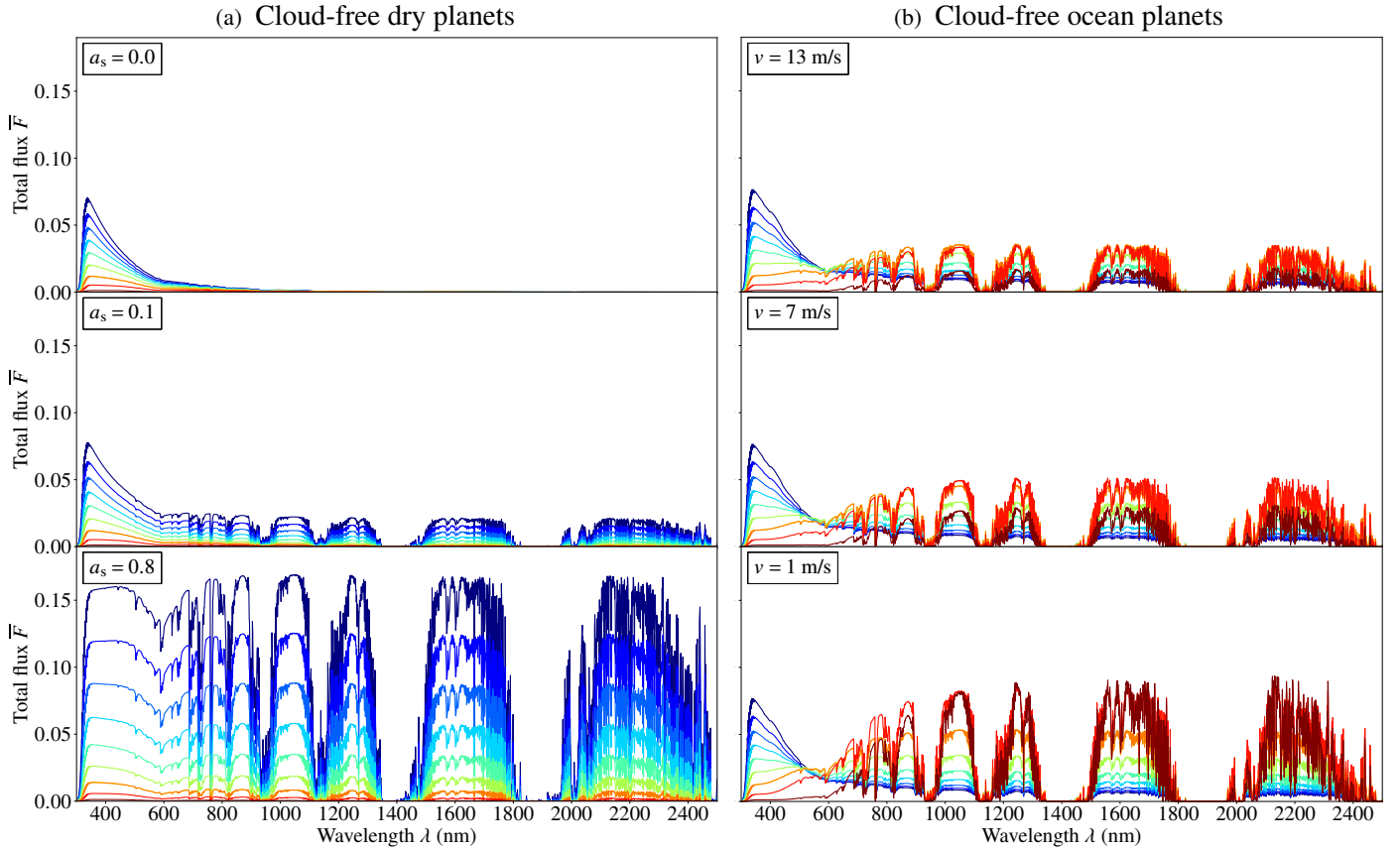
(a) Cloud-free dry planets　　　(b) Cloud-free ocean planets

Fig. 9. Total flux $\overline{F}$ of starlight that is reflected by cloud-free, dry model planets (*left column*) and cloud-free ocean planets (*right column*) as functions of λ at 1 nm resolution, for nine phase angles α from 90° (dark blue) to 170° (dark red) with steps of 10° (see Fig. 8 for the colors of the different α's). The surface albedo a_s of the dry planets is 0.0 (*top left*), 0.1 (*middle left*), and 0.8 (*bottom left*). The wind speed v over the oceans is 13 m s^{-1} (*top right*), 7 m s^{-1} (*middle right*), and 1 m s^{-1} (*bottom right*).

by CH$_4$ (e.g., near 2300 nm) is more difficult to distinguish by eye because of its less distinctive absorption bands and nearby H$_2$O vapor absorption features (cf. Fig. 4).

Figure 9b shows $\overline{F}$ that is reflected by cloud-free planets with ocean surfaces over the same spectral range and at the same phase angles. The wind speed v decreases in the subfigures from 13 m s^{-1} at the top, to 1 m s^{-1} at the bottom. At $v = 1$ m s^{-1}, the glint is the narrowest but also the brightest (directionally reflecting and polarizing) (see Fig. 7 of Trees & Stam 2019).

At $\alpha = 90°$, ocean planets are relatively dark and their $\overline{F}$ spectrum is thus comparable to that of a dry planet with a low surface albedo (cf. Fig. 9a for $a_s = 0$ and 0.1). Compared to the dry planet with $a_s = 0$, $\overline{F}$ at $\alpha = 90°$ of an ocean planet is slightly larger at $\lambda \lesssim 550$ nm, with a small bump between 300 and 500 nm, because of the natural blue color of our model ocean (cf. Fig. 7). For a discussion of the influence of the ocean color on $\overline{F}$ at various α, we refer to Fig. 5 in Trees & Stam (2019). At longer wavelengths and outside the absorption bands, the ocean glint enhances $\overline{F}$. At $\alpha = 90°$, the contribution of the glint to $\overline{F}$ is virtually independent of the wind speed: the contribution of a narrow, bright glint is approximately equal to that of a wide, dim glint when integrated over the cloud-free planetary disk for $\alpha \lesssim 135°$ (see also Sect. 3.1.2 of Trees & Stam 2019).

Wind speed dependent differences in $\overline{F}$ could also be due to the larger contribution of the foam on the surface for higher wind speeds (see Fig. 6). Because the visibility of the ocean surface decreases with increasing α because of the increasing average

optical path lengths through the atmosphere, we expect the signature of foam to be most apparent at $\alpha = 90°$ in Fig. 9b. Indeed, for example at 865 nm, where there is relatively little absorption, a small increase of $\overline{F}$ is seen for $\alpha = 90°$ and $v = 13$ m s^{-1} ($\overline{F} = 0.0111, 0.0103,$ and 0.0103 for $v = 13, 7,$ and 1 m s^{-1}, respectively). However, this weak foam signature in $\overline{F}$ can easily be confused with other signatures that shape $\overline{F}$ of a planet in the continuum, such as surface reflection (Fig. 9a) and clouds (see Sect. 3.1.2).

With increasing α from 90° to 160°, $\overline{F}$ in Fig. 9b increases for $\lambda \gtrsim 400$ nm outside the absorption bands compared to $\overline{F}$ of a dry planet with a black surface ($a_s = 0$). This α-dependent increase is the result of increasing Fresnel reflection of direct starlight (i.e., a brighter glint), due to the increasing local reflection angles on the waves (see Sect. 2.3.2). When $\lambda \gtrsim 900$ nm and outside absorption bands, this contribution of the glint is spectrally more or less flat (cf. Fig. 7). The spectrally flat glint serves as a continuum with superimposed gaseous absorption bands: in the bands, direct starlight is absorbed and does not reach the ocean surface or is absorbed after being reflected by the ocean, thus decreasing the visibility of the glint.

For $\lambda \lesssim 900$ nm outside absorption bands, the α-dependent glint contribution disappears gradually with decreasing λ (see Fig. 9b) as the atmospheric optical thickness increases and less light reaches the surface. Consequently, the $\overline{F}$ spectra of an ocean planet at the different values of α intersect between about 500 and 700 nm. These results are consistent with the intersecting
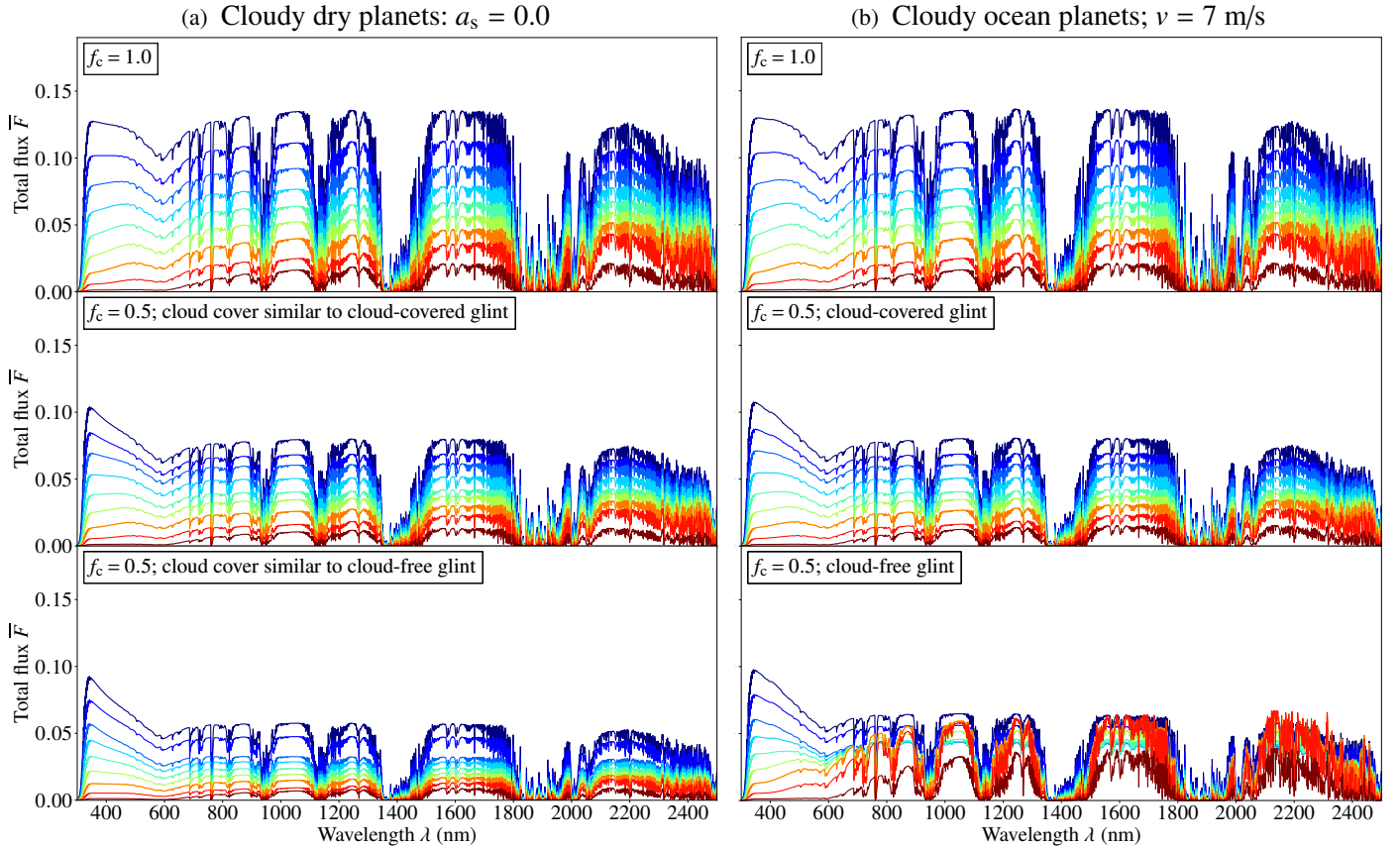
Fig. 10. Similar to Fig. 9, except with clouds. The cloud coverage fraction f_c = 1.0 (*top*) or 0.5 (*middle and bottom*). The *middle figures* have similar patchy cloud patterns, chosen such that the glint of the ocean planet (*right*) is fully covered. The *bottom figures* also have similar patchy cloud patterns, but chosen such that the glint of the ocean planet is cloud-free.

planetary phase curves of cloud-free ocean planets at various (roughly absorption-free) wavelengths between 350 and 865 nm in Fig. 1 of Trees & Stam (2019).

3.1.2. $\overline{F}$ of cloudy planets

Figures 10a and b show the spectra of $\overline{F}$ that is reflected by dry and ocean planets, respectively, for cloud coverage fractions, f_c, equal to 1.0, that is, the planet is completely covered by clouds (top), and 0.5 (middle and bottom). On the cloudy dry planets, a_s = 0.0, and on the cloudy ocean planets, v = 7 m s^{-1}. Compared to their cloud-free equivalents (the top of Figs. 9a and b), the clouds increase $\overline{F}$ at all wavelengths outside the absorption bands. Because for f_c = 1, the ocean glint is fully covered by the optically thick clouds, the spectra for the cloudy dry and cloudy ocean planets are virtually the same at each α: there is no ocean-glint-related increase in $\overline{F}$ with increasing α, nor a small bump in $\overline{F}$ between 300 and 500 nm related to the blue water color.

In the middle row of Figs. 10a and b, f_c = 0.5, and the patchy cloud pattern is such that on the ocean planets, the glint is fully covered by clouds (see the right image in Fig. 2). For comparison, the cloud pattern on the dry planet is similar to that on the ocean planet. When the glint is covered by clouds, there is no increase of $\overline{F}$ with increasing α. Only a very subtle remnant of the ocean color bump near $\lambda \sim$ 400 nm is visible at α = 90°, which is caused by light that is reflected by the ocean in between the cloud patches.

In the bottom row of Figs. 10a and b, f_c is also 0.5, but here the patchy cloud pattern leaves the ocean glint uncovered (see the left image in Fig. 2). The uncovered glint significantly enhances $\overline{F}$ with increasing α outside the absorption bands. Because of the decreasing optical thickness of the gaseous atmosphere with increasing λ, some $\overline{F}$ spectra for various α intersect. The different cloud patterns also influences the spectra of the dry planets: the "glint region" is at the well-illuminated, well-visible equator, so with a dark and dry planet, a cloud-free glint-region results in a smaller $\overline{F}$.

From Figs. 10a and b, we conclude that the detectability of an ocean glint in $\overline{F}$ is not directly limited by the cloud coverage fraction f_c. Instead, it strongly depends on the spatial distribution of the clouds, in particular on the coverage of the glint.

3.2. Polarized flux $\overline{Q}$

3.2.1. $\overline{Q}$ of cloud-free planets

Figures 11a and b are similar to Figs. 9a and b, except for the polarized flux $\overline{Q}$. The obvious difference in $\overline{Q}$ between dry and ocean planets is that for all wind speeds v and for α between 90° to 150°, ocean planets show an enhancement of $|\overline{Q}|$ with increasing α at all λ outside absorption bands and intersections of the $\overline{Q}$ spectra at various values of α between ~600 and ~900 nm, while for the dry planets, there is only a noticeable polarized flux for $\lambda \lesssim$ 1000 nm, and the $\overline{Q}$ spectra do not intersect at any α, regardless of the surface albedo a_s.
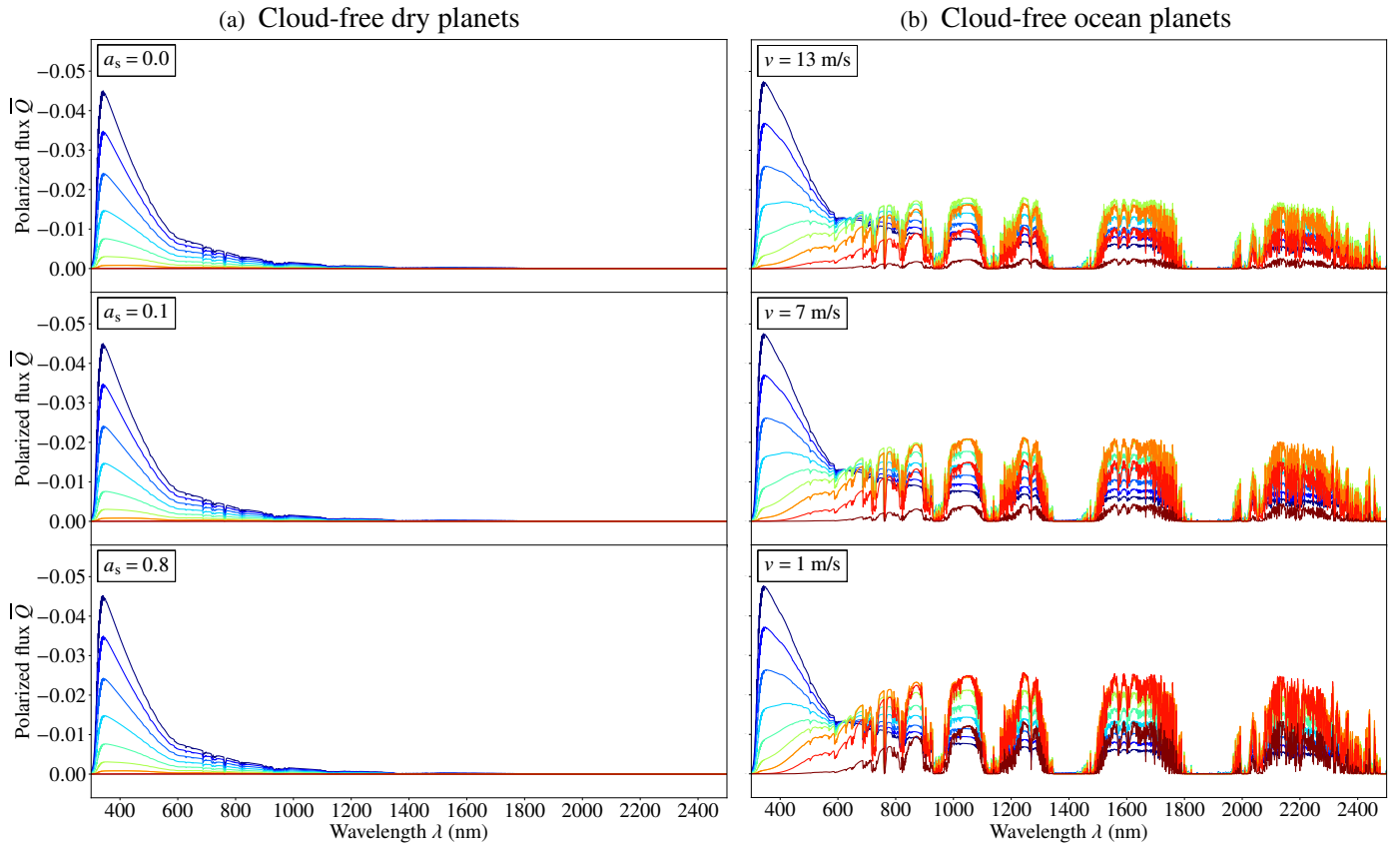
(a) Cloud-free dry planets

(b) Cloud-free ocean planets

Fig. 11. Similar to Fig. 9, except for the linearly polarized flux $\overline{Q}$. Note the inverted vertical axis!

(a) Cloudy dry planets; $a_s = 0.0$

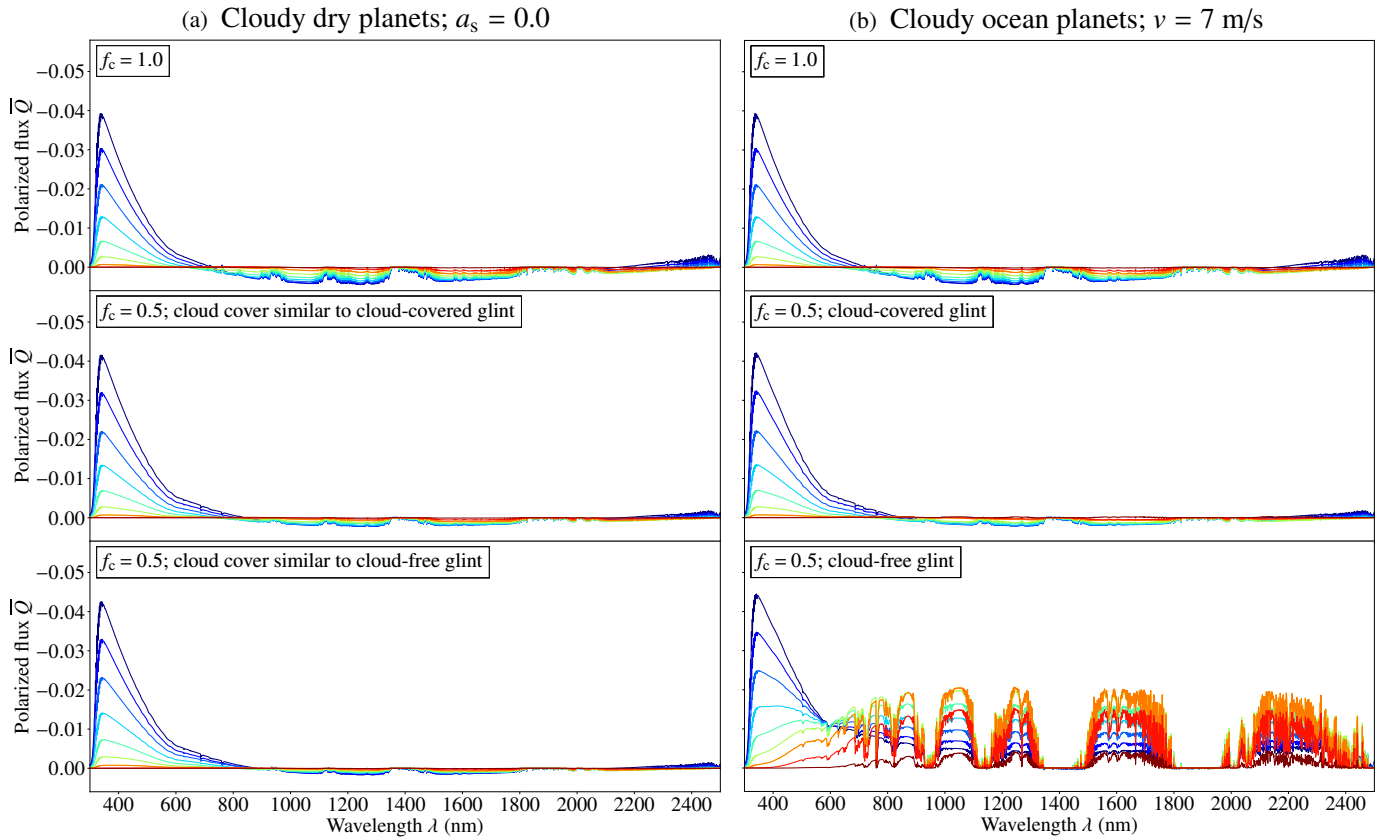(b) Cloudy ocean planets; $v = 7$ m/s

Fig. 12. Similar to Fig. 10, except for the linearly polarized flux $\overline{Q}$.

The enhancement of $|\overline{Q}|$ with increasing α outside absorption bands for cloud-free ocean planets is due to the increasing polarized Fresnel reflection of direct starlight with increasing local reflection angles on the ocean waves. The intersections of the $\overline{Q}$ spectra for various α's is caused by the spectral dependence of the scattering by the gas. At the shortest wavelengths, the polarized radiance is determined by Rayleigh scattering and hence is strongly α dependent, while with increasing λ, the atmospheric scattering decreases and the visibility of the polarized ocean glint increases. The very small values of $|\overline{Q}|$ of the dry, cloud-free planets for $\lambda \gtrsim 1000$ nm are due to the absence of a significant polarizing scatterer or reflector at those wavelengths, as the Rayleigh scattering optical thickness is very small and as the surface reflection is unpolarized.

For the cloud-free ocean planets, $\overline{Q}$ outside the absorption bands seems virtually independent of the wind speed v for $\alpha = 90°-120°$. At $\alpha = 90°$, the suppression of the Fresnel reflection by the open ocean surface due to foam leaves a negligibly small decrease of $|\overline{Q}|$ for $v = 13$ m s^{-1} with respect to $v = 7$ m s^{-1} (e.g., 1.04×10^{-4} at $\lambda = 865$ nm). Indeed, Fig. 4 of Trees & Stam (2019) shows that $|\overline{Q}|$ only depends on v for $\alpha \gtrsim 123°$ as there the glint is increasingly dominant in the signal. In Fig. 11b, the strongest enhancement of $|\overline{Q}|$ is at $\alpha = 140°$ for $v = 13$ m s^{-1}, and at $160°$ for $v = 1$ m s^{-1}. Figure 4 of Trees & Stam (2019) shows that with decreasing v, $|\overline{Q}|$ at a NIR wavelength ($\lambda = 865$ nm) peaks at a larger α, which is explained by the brighter but narrower glint for smaller v, that is also less affected by wave shadows.

Similar to $\overline{F}$ of the cloud-free ocean planet, the glint in the near-infrared $\overline{Q}$ has a spectrally approximately flat continuum with superimposed gaseous absorption features. Inside absorption bands, less direct light reaches the ocean and/or the observer after being reflected, resulting in a smaller $|\overline{Q}|$. For example, absorption features of O_2 and CO_2 can be identified in $|\overline{Q}|$ at 1270 and 1600 nm, respectively.

3.2.2. $\overline{Q}$ of cloudy planets

Figures 12a and b are similar to Figs. 10a and b, except for the polarized flux $\overline{Q}$. For completely cloudy planets ($f_c = 1.0$), $\overline{Q}$ is, like the total flux, virtually similar for dry and ocean planets: the thick clouds cover the ocean signatures and at $\lambda \lesssim 700$ nm, $\overline{Q}$ is determined by the Rayleigh scattering of the gas above (and to a lesser extent inside and below) the clouds. At $\lambda \sim 700$ nm, the direction of polarization can be seen to change: the sign of $\overline{Q}$ changes from negative to positive because at the longer wavelengths the scattering by the cloud particles overtakes the Rayleigh scattering, and the single scattering matrix element F_{21} of the water cloud droplets is positive at small to intermediate scattering angles Θ, thus at intermediate to large phase angles α (see Fig. 5). The sign change in Figs. 12a and b is most apparent at $\alpha = 90°$, because with increasing α from $90°$, the observable fraction of the planetary disk decreases, thus the absolute amount of flux decreases, and in addition, the degree of polarization of the light that is singly scattered by the cloud droplets generally decreases with decreasing Θ (Fig. 5). For $\lambda \gtrsim 2100$ nm, the sign of F_{21} of the droplets, and consequently the sign of $\overline{Q}$, changes again.

For the planets with patchy clouds ($f_c = 0.5$) that cover the glint (the middle row of Figs. 12a and b), the sign changes of $\overline{Q}$ are somewhat less apparent because there are simply less

scattering cloud particles across the planet. With the glint covered by patchy thick clouds, the ocean planets have virtually similar $\overline{Q}$ spectra as the dry planets: no ocean signatures can be identified.

In case the glint is not covered by clouds (the bottom row of Figs. 12a and b), the $\overline{Q}$ spectra of the ocean planet differ significantly from those of the similarly clouded dry planet: with increasing α up to $150°$, the glint increases $|\overline{Q}|$ outside the absorption bands as compared to $|\overline{Q}|$ of the dry planet. The latter spectra are almost unaffected by a different cloud pattern: $|\overline{Q}|$ at $\lambda \lesssim 800$ nm is only slightly increased because the equatorial regions are mostly cloud-free, such that relatively more signal is received from regions where Rayleigh scattering gas dominates the local signals.

Comparing Figs. 11 and 12 at NIR wavelengths ($\lambda > 800$ nm) outside absorption bands shows that, for all dry planets, $\overline{Q}$ is close to zero or slightly positive, while for all ocean planets with a cloud-free glint, $\overline{Q}$ is negative. Moreover, for the latter planets, $|\overline{Q}|$ increases with increasing α, causing the $\overline{Q}$ spectra for the different values of α to intersect. The negative $\overline{Q}$ at NIR wavelengths and the intersecting $\overline{Q}$ spectra for various α could reveal the presence of an ocean.

3.3. Degree of polarization P_s

3.3.1. P_s of cloud-free planets

Figure 13a is similar to Figs. 9a and 11a, except for P_s. Between 300 and 1000 nm, the results agree well with earlier published polarization spectra by Stam (2008) (the latter do not go beyond 1000 nm). For dry planets with a black surface ($a_s = 0.0$), P_s is highest around $\alpha = 90°$ due to Rayleigh scattering. Because of multiple scattering of light, P_s decreases with decreasing λ and increasing gaseous scattering optical thickness from the visible toward the ultraviolet, reaching a local minimum at ~320 nm (see also Fig. 3 of Stam 2008). At shorter wavelengths, absorption by O_3 (the Huggins band) suppresses multiple scattering, which leads to an increase of P_s (see, e.g., Stam 2008; Aben et al. 1999). Although P_s in the near-infrared or in the Huggins band is relatively high due to single scattering of light by the atmospheric gas above the black surface, the polarized flux $|\overline{Q}|$ is very small at those wavelengths due to the small gaseous scattering optical thickness and the absorption (cf. Fig. 11a).

Even a little bit of reflection by the surface ($a_s = 0.1$) influences P_s significantly, as unpolarized light is added to the planet's signal, decreasing P_s outside the absorption bands. In particular at the longer wavelengths, this decrease is significant, because the polarized flux $|\overline{Q}|$ from light that has been singly scattered by the atmospheric gas is very small (see Fig. 11a). A similar, but stronger decrease of P_s is found for the dry planet with a bright surface ($a_s = 0.8$).

The P_s spectra of the cloud-free dry planets with nonblack surfaces show absorption band features, mostly due to O_2 and H_2O (see Fig. 4). Inside those absorption bands, P_s is high compared to outside the bands, because the absorption prevents light to reach the reflecting surface and any unpolarized light that is reflected by the surface to reach the observer, leaving the strongly polarized signal of single Rayleigh scattering in the P_s spectra. Indeed, in the bands, P_s reaches its single scattering value, as if the surface were black (top row). The absorption of light by gases in the cloud-free atmospheres of dry exoplanets with reflecting surfaces thus shows up as peaks in the P_s spectra (e.g., Stam 2008, and references therein).
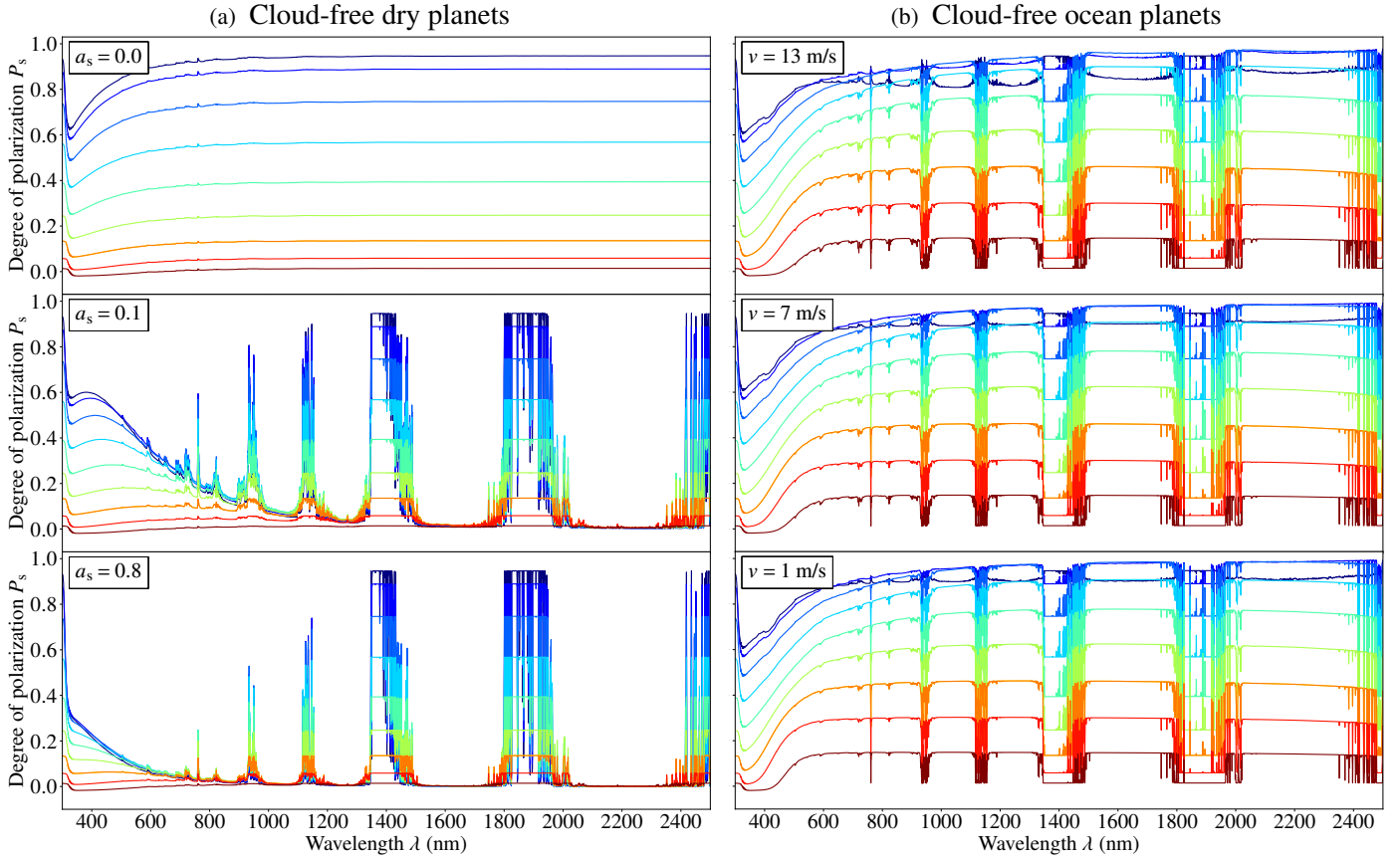
(a) Cloud-free dry planets

(b) Cloud-free ocean planets

Fig. 13. Similar to Fig. 9, except for the degree of polarization P_s.

(a) Cloudy dry planets; $a_s = 0.0$
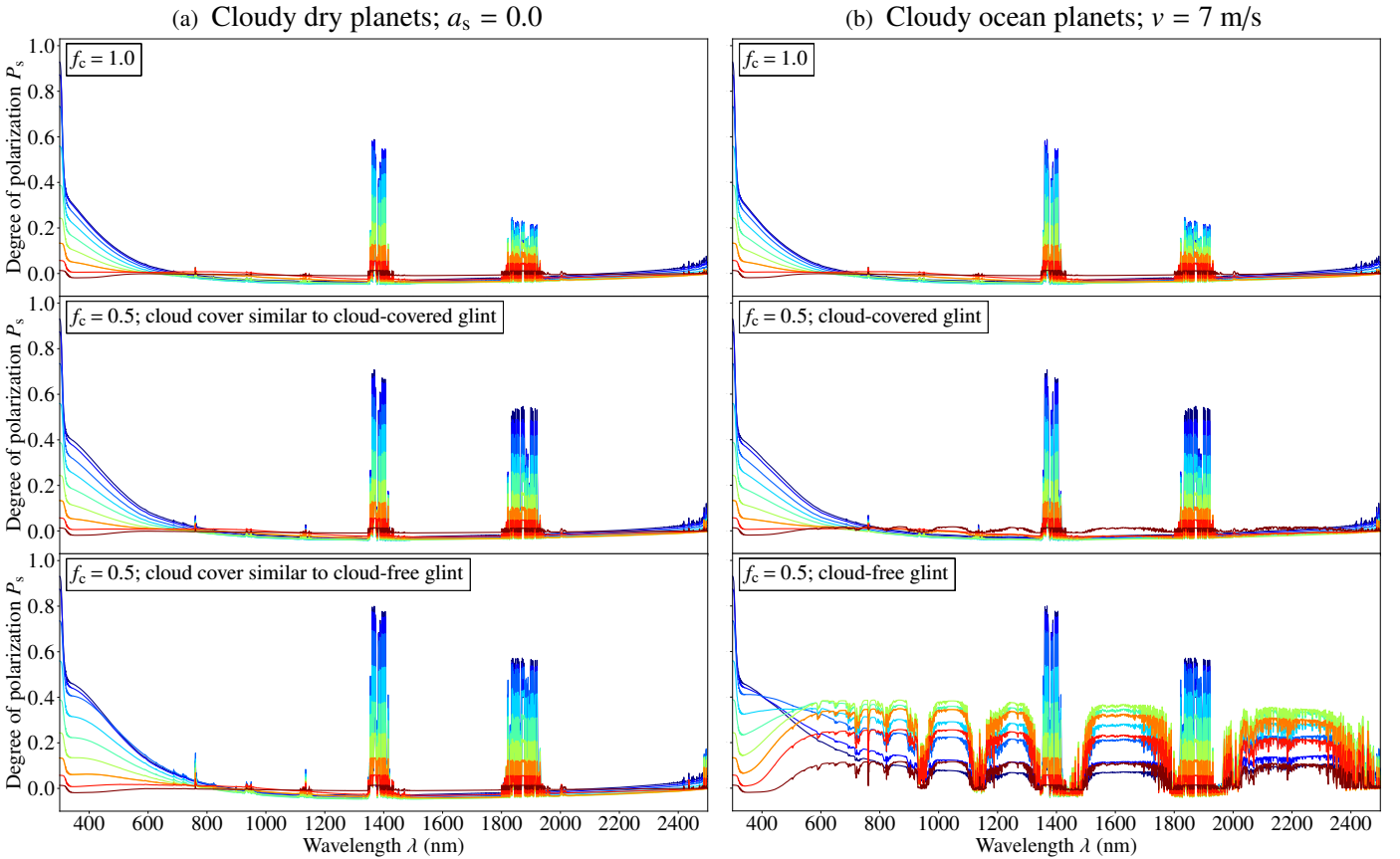
(b) Cloudy ocean planets; $v = 7$ m/s

Fig. 14. Similar to Fig. 10, except for the degree of polarization P_s.

Figure 13b shows P_s of cloud-free ocean planets. At first sight, and outside the absorption bands, these spectra look rather similar to those of the cloud-free dry planet with a black surface, but there are some profound differences, three of which we discuss below.

Firstly, at the shortest wavelengths, the optically thick atmosphere prevents Fresnel reflected light from the ocean surface to reach the observer directly, but weakly polarized light that is diffusely reflected by the ocean still slightly decreases P_s (see also Fig. 5 of Trees & Stam 2019). The bump in the ocean reflection between 300 and 500 nm (see Fig. 7) adds somewhat more unpolarized light to the planet signal, as is most apparent from the small dip in P_s for $\alpha = 90°$ (at that phase angle, the contribution of the blue ocean is larger than at larger phase angles, as the optical paths through the planet's atmosphere increase with increasing α).

Secondly, for the cloud-free ocean planets, the maximum P_s does not occur at $\alpha = 90°$, like for the cloud-free dry planet, but at larger values of α. The reason is that with increasing λ, the influence of the Fresnel reflecting ocean increases, shifting the maximum P_s from that of the Rayleigh scattering to the phase angle corresponding to the local Brewster angle, that is given by $\alpha_B = 2 \arctan(n_{\text{water}}/n_{\text{air}})$ (see Fig. 1 Trees & Stam 2019). For example, at 1000 nm, $\alpha_B = 106°$, while at 2500 nm $\alpha_B = 107°$. Consequently, the P_s spectrum at $\alpha = 90°$ intersects with the spectra at $\alpha = 100°$ and $110°$. Because P_s of the cloud-free ocean planet peaks at larger α, the P_s-continua of cloud-free ocean planets are higher than those of the cloud-free dry black planet for $\alpha > \alpha_B$. As can be seen in Fig. 13b, a high wind speed ($v = 13$ m s^{-1}) causes an extra decrease of the P_s spectrum for $\alpha = 90°$ and $100°$, due to the sea foam that covers 2.46% of the ocean when $v = 13$ m s^{-1}. The foam suppresses P_s because it lowers the contribution of the (polarized) Fresnel reflection and it diffusely reflects unpolarized light. As the sea foam albedo decreases toward longer wavelengths, the latter suppressing effect also decreases with wavelength (at 1000 nm and $v = 13$ m s^{-1}, P_s decreases with 0.081 with respect to $v = 7$ m s^{-1}, while at 2200 nm, it decreases with 0.037). As the optical paths through the exoplanet's atmosphere increase with increasing α, the influence of the foam on P_s is more apparent for smaller α (see Appendix B of Trees & Stam 2019).

Thirdly, at wavelengths where the influence of the Fresnel reflecting ocean dominates that of the atmosphere ($\lambda \gtrsim 600$ nm), P_s is lower in the absorption bands than outside for all wind speeds. These dips of P_s (instead of the peaks for the dry planets) are explained as follows. Inside the absorption bands, P_s is close to its single scattering value for the given scattering geometry, which is similar to P_s for the cloud-free dry planet with a black surface ($a_s = 0$). Outside the absorption bands, P_s for the ocean planet is determined by the strongly polarized fluxes of the ocean glint (Fig. 11b). As discussed above, for $\alpha > \alpha_B$, this P_s is higher than the P_s of the cloud-free, dry planet with a black surface. Thus, for $\alpha > \alpha_B$, the gaseous absorption bands show up as dips in the P_s spectra of cloud-free ocean planets.

3.3.2. P_s of cloudy planets

Figures 14a and b are similar to Figs. 10a and b, and 12a and b, except for P_s. As before, for completely cloudy planets ($f_c = 1.0$), the P_s spectra of the dry and ocean planets are virtually the same because the clouds cover the ocean. The polarization for $\lambda \lesssim 700$ nm is due to Rayleigh scattering (see the discussion of Figs. 12a and b). And, similar to the sign change of $\overline{Q}$, P_s

changes sign near $\lambda \sim 700$ nm because of the influence of light that is scattered by the clouds (see Sect. 3.2).

Because of multiple scattering of light between the cloud droplets, the optically thick clouds reflect strongly depolarized light, just like the surfaces with nonzero albedos (cf. $a_s = 0.1$ and $a_s = 0.8$ in Fig. 13a). The main difference between the effect of a bright surface and a thick cloud deck is due to the altitude at which the light is reflected: the cloud deck extends up to 4 km and thus covers a large fraction of the H_2O molecules as those are concentrated in the lowest atmospheric layers. Therefore, the H_2O absorption band features in P_s of cloudy planets are generally less strong than in P_s of cloud-free planets with nonzero a_s. Only in the strongest absorption bands (e.g., ~1400 nm and ~1900 nm), P_s reaches the single scattering values, resulting in spectral peaks.

The P_s spectra of half-cloudy ($f_c = 0.5$) dry and ocean planets with the glint on the latter covered by clouds, are virtually the same (middle row of Figs. 14a and b): no ocean signature can be identified.

When the glint is cloud-free, however, the P_s spectra of the dry and ocean planets differ significantly as can be seen in the bottom row of Figs. 14a and b. Outside the absorption bands, P_s is enhanced due to the Fresnel reflecting ocean. The enhancement increases with α up to $140°$ just like the polarized flux $|\overline{Q}|$. The value of P_s outside the bands does not reach the value for the cloud-free ocean planet (Fig. 13b) because the cloud patches add unpolarized flux to the planetary signal. However, the values of P_s outside the bands are still larger than those for the cloud-free, dry planet with a black surface, suggesting that the value of P_s outside absorption bands could reveal the presence of an ocean.

Interestingly, when patchy clouds surround (but not cover) the glint, the dips of P_s at absorbing wavelengths can still be identified (see Fig. 14b). In fact, it could be argued that patchy clouds enable the detection of this ocean signature because with clouds, the dips in P_s appear already at smaller α's, such as $90°$ and $100°$, and the dips are wider and already apparent at shorter λ, compared to the case for the cloud-free ocean planets (Fig. 13b). In the H_2O absorption bands, the polarizing glint is invisible to the observer, but the clouds are not. In the bands, P_s attains similar values as for the dry planet with a black surface and similar patchy clouds (Fig. 13a). In the deepest bands, the clouds are also invisible and for each α, P_s returns to the value of single Rayleigh scattering.

Comparing Figs. 13a and b, and 14a and b, we find that for all dry planets, with black or bright surfaces, and with or without clouds, P_s in gaseous absorption bands is either close to its continuum value, or higher. For dry planets, P_s is thus either flat or shows peaks in absorption bands. Dips in P_s are only observed for ocean planets and only when the glint is cloud-free.

4. Discussion of absorption peaks and dips in P_s

Here, we further analyze and discuss the influence of atmospheric parameters on the peaks and dips in P_s at wavelengths inside gaseous absorption bands. We focus on absorption by H_2O vapor between 850 and 1000 nm. The wind speed v over the oceans is 7 m s^{-1} and the dry planets have black surfaces ($a_s = 0.0$).

Figure 15a shows the computed P_s of starlight that is reflected by cloud-free ($f_c = 0.0$) ocean planets and dry planets, similar as in Fig. 13, but here we have added lines for halved and doubled H_2O vapor volume mixing ratios (VMRs). The
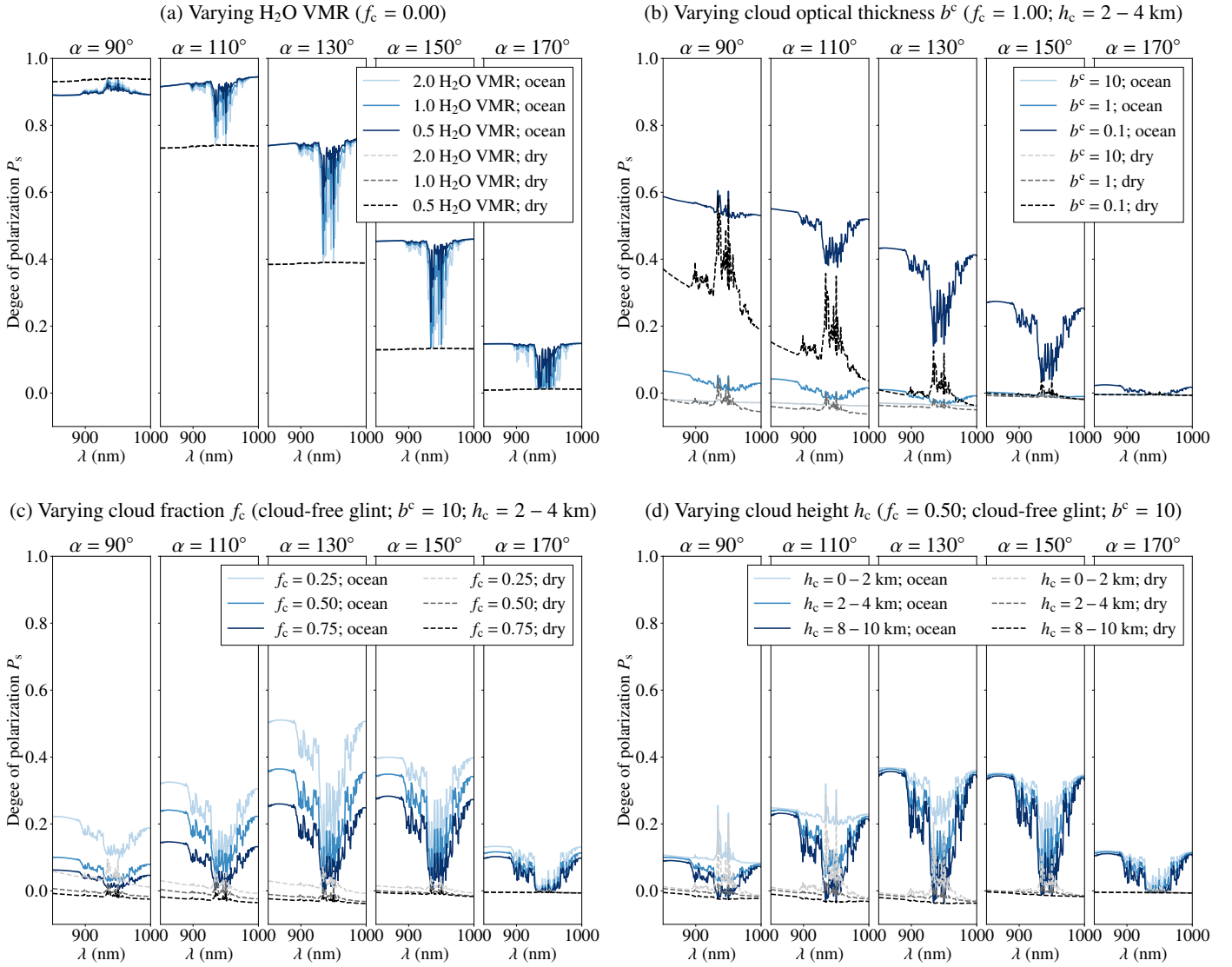
Fig. 15. Computed degree of polarization P_s of starlight reflected by planets with ocean surfaces (solid blue lines) or dry surfaces (dashed black lines), and different atmospheres (different line color darkness), with h_c indicating the vertical extent of the clouds, presented at five planetary phase angles α from 90° to 170°. The wind speed v over the oceans is 7 m s^{-1}. The dry planets have black surfaces ($a_s = 0.0$). In Fig. 15a, the lines for the dry planets with various H$_2$O VMRs virtually overlap.

results are presented at five phase angles α: 90°, 110°, 130°, 150°, and 170°. For the cloud-free ocean planet, the dip in P_s decreases (increases) with a decreased (increased) H$_2$O VMR. For the cloud-free dry planet, the P_s spectrum across the absorption band is virtually flat for all values of the H$_2$O VMR, because for this planet and at these long wavelengths, P_s is determined by single Rayleigh scattering both outside and inside the band.

Figure 15b is similar to Fig. 15a, except with the standard H$_2$O VMR and here the planets are completely covered by clouds ($f_c = 1.0$) with an optical thickness $b^c = 10$ (at 550 nm), similar as in Fig. 14, but also for $b^c = 0.1$, and 1.0. Generally, the smaller b^c, the higher the continuum P_s, because there is less unpolarized flux from the clouds. For the dry planets, the clouds act as a depolarizing reflecting surface (cf. Fig. 13a), resulting in peaks in P_s across the absorption bands, where the clouds are less visible. For the ocean planets, the continuum P_s increases with decreasing b^c, as the polarized flux from the glint that penetrates the clouds increases. And while an optically thick cloud covering the glint leaves P_s featureless across the absorption

band, an optically thinner cloud transmits the glint and creates a dip in P_s. In fact, the thin cloud ($b^c = 0.1$) covering the glint makes the dip in P_s even more apparent.

Figure 15c is similar to Fig. 15b, except here the planets have patchy clouds (all with $b^c = 10$ at 550 nm), for different cloud coverage fractions f_c, namely 0.25, 0.50, and 0.75. For all coverages, the glint is cloud-free. It can be seen that increasing f_c decreases P_s outside the absorption bands, because it increases the unpolarized flux. However, even for a heavily cloudy planet ($f_c = 0.75$), an ocean will leave a dip in P_s when the glint is cloud-free.

Figure 15d, finally, shows P_s for dry and ocean planets with patchy clouds ($f_c = 0.50$) and a cloud-free glint, but for clouds at different altitudes h_c. While on the standard planets the clouds extend from 2 to 4 km, here, we have included curves for lower ($h_c = 0-2$ km) as well as higher ($h_c = 8-10$ km) clouds. Increasing the cloud altitude hardly affects P_s in the continuum because at these long wavelengths, there is almost no Rayleigh scattering above the clouds anyway. The dip in P_s, however, deepens
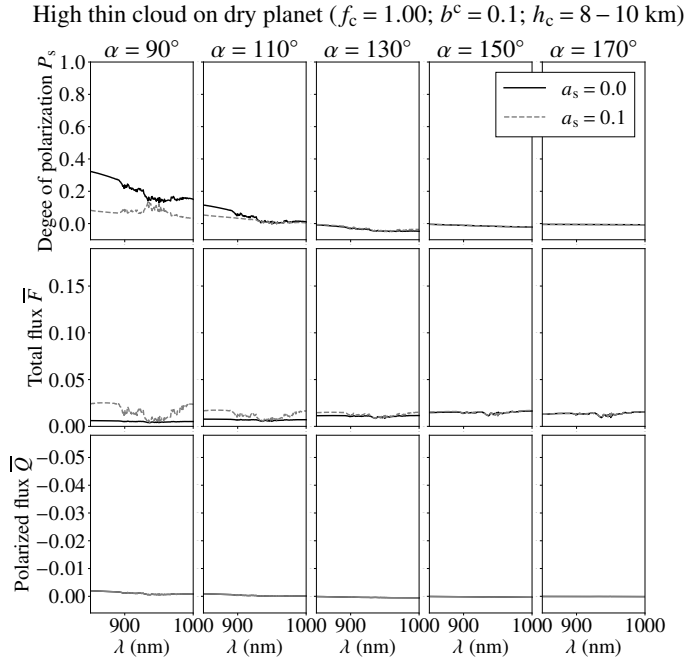
High thin cloud on dry planet ($f_c = 1.00$; $b^c = 0.1$; $h_c = 8 - 10$ km)

Fig. 16. Computed degree of polarization P_s, total flux $\overline{F}$ and polarized flux $\overline{Q}$ of starlight reflected by dry planets with black surfaces, thus with $a_s = 0.0$ (black solid lines), and dark surfaces, with $a_s = 0.1$ (gray dashed line), and a high ($h_c = 8-10$ km) and optically thin ($b^c = 0.1$) water cloud, presented at five planetary phase angles α from 90° to 170°.

as the amount of H_2O gas above the clouds and thus the absorption optical thickness decreases, and the contribution of the low polarization of the clouds increases inside the band.

Figure 15 convincingly shows that the depth and shape of the dip in P_s depend on the H_2O VMR, and on the optical thickness b^c, coverage fraction f_c, and altitude h_c of the clouds. However, in all our model computations, a dip in P_s instead of a peak only occurs in the presence of an ocean. Such dips in P_s could thus reveal the presence of an ocean.

We note that dips in P_s of light that is locally reflected by an Earth-like gaseous atmosphere with a high aerosol layer above a black surface were found by Stam et al. (1999) (see their Fig. 13 for the effect of stratospheric H_2SO_4 aerosol on the shape of the O_2A band in P_s). Also, Emde et al. (2017) computed dips in P_s of light reflected by dry black surface planets at $\alpha = 90°$ with a high, thin ice cloud (see their Fig. 7). Indeed, we also find a dip in P_s between 850 and 1000 nm for a dry planet with a black surface at $\alpha = 90°$ if we place a thin ($b^c = 0.1$) layer of water cloud droplets between altitudes of 8 and 10 km, as shown in Fig. 16. However, contrary to what we find for ocean planets, total flux $\overline{F}$ and polarized flux $\overline{Q}$ are extremely small in that case and the dip in P_s vanishes with increasing α. This potentially false ocean signature in P_s also vanishes when a small amount of unpolarized flux is added to the signal, for example, due to reflection by a nonblack surface, for instance when $a_s = 0.1$.

A detection of dips in the measured P_s spectrum of the sunlight that is reflected by the Earth when the glint is cloud-free would confirm our model predictions, and could already be done at a single phase angle. Assuming the depolarization by the lunar surface is spectrally smooth across gaseous absorption bands, those dips can be searched for in Earth-shine observations. Sterzik et al. (2012, 2019) mainly reported peaks in Earth-shine spectra of P_s measured between 420 and 920 nm. In some P_s spectra of Sterzik et al. (2019), dips can be seen

in the O_2A band, although they are not discussed. Our simulations show that the near-infrared wavelength range could be more suitable to search for dips in P_s, since those dips should be deeper and spectrally wider than the dips at shorter wavelengths. Miles-Páez et al. (2014) took Earth-shine measurements of P_s in the near-infrared and reported peaks across H_2O absorption bands near 930 and 1120 nm, which could suggest that at the time of the observations, a continent or cloud covered the glint. More spectropolarimetric Earth-shine measurements in the near-infrared over longer time periods, in which the cloud coverage of the glint can vary, are needed to confirm our predicted ocean signatures.

5. Comparison with earlier work

All our model computations show that P_s dips instead of peaks in gaseous absorption bands only in the presence of an ocean. Such dips in P_s could thus reveal an ocean. These spectropolarimetric ocean signatures are absent in the computed spectra of planets with oceans by Stam (2008), because in that paper, the oceans had flat surfaces, not rough, wavy ones that broaden the glint and cast shadows. With a flat interface and monodirectional incident starlight (thus when the distance between the star and the planet is much larger than the radius of the planet), the glint is infinitely narrow as it is the reflected direct starlight and hence a mirror image of the star. This infinitely narrow glint is lost upon integration over the planetary disk. We note that the diffuse sky-light that is reflected by a flat interface will still contribute to the planet's signal. Another difference between the ocean model in this paper and the one used in Stam (2008) is that our ocean has a natural blue color and sea foam (see Sect. 2.3.2), while the ocean in Stam (2008) is black.

Figure 17 shows our computed $\overline{F}$, $\overline{Q}$, and P_s for cloud-free ocean planets, similar as in Figs. 9b, 11b and 13b, except for $v = 1$ m s^{-1}, compared to the results of Stam (2008), for λ ranging from 300 to 1000 nm and at $\alpha = 90°$, 120°, and 150°. At 90°, the bump in $\overline{F}$ and the dip in P_s near $\lambda = 400$ nm are absent in the spectra of Stam (2008) because they are caused by the ocean's blue color. For $\alpha = 120°$ and 150°, the bump and dip are increasingly weaker in our spectra because of the longer average optical paths through the optically thick atmosphere at those short wavelengths, which decreases the amount of light that reaches the ocean.

At the longer wavelengths, where the atmospheric scattering optical thickness is small, and outside absorption bands, the ocean glint strongly increases our $\overline{F}$, $|\overline{Q}|$, and P_s with increasing α from 90° as compared to the results from Stam (2008). This increase is caused by the increase of the local reflection angles on the ocean waves, and with that by the increase of Fresnel reflection and the glint brightness.

For accurate modeling of the signatures of oceans on exoplanets, the glint on the waves appears to be very important. The influence of the waves depends significantly on the pattern of the clouds: if the glint is cloud-free, it leaves clear signatures in the spectra of $\overline{F}$, $\overline{Q}$, and P_s. If the glint is covered by clouds, the signature disappears, unless the cloud patch is optically thin. It is thus important to use horizontally inhomogeneous cloud patterns when modeling spectra of exoplanets with patchy clouds and oceans. Indeed, for this modeling, a weighted sum of a cloud-free and a completely cloudy planet to model partly cloudy planet signals (as used by, e.g., Stam 2008; Zugger et al. 2010, 2011; Emde et al. 2017) would fail to fully represent an actual planet signal. This is illustrated in Fig. 18, where we use
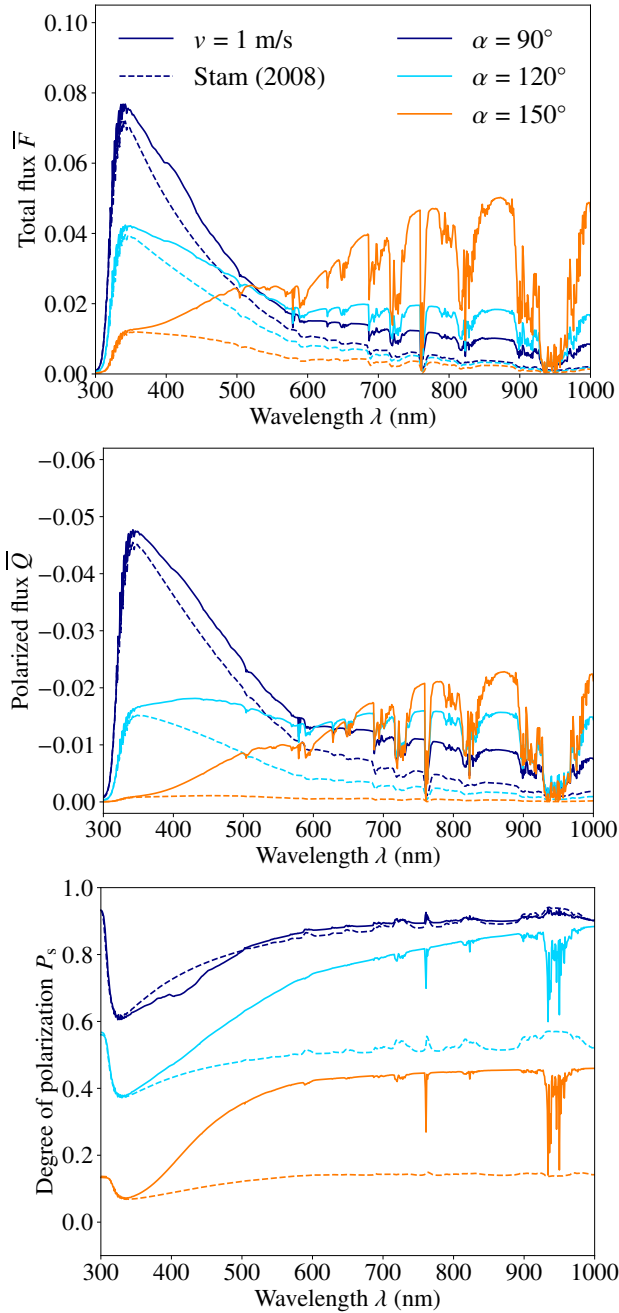
Fig. 17. Comparison of our results (solid lines) to the results of Stam (2008) (dashed lines) for the computed total flux $\overline{F}$, polarized flux $\overline{Q}$, and degree of polarization P_s of light that is reflected by cloud-free ocean planets at $\alpha = 90°$, $120°$, and $150°$. Our ocean planet has a natural blue color and a glint (for $v = 1$ m s^{-1}). The ocean model of Stam (2008) is black and flat, and while its interface is a Fresnel-reflector, the lack of waves results in an infinitely narrow glint.

Cloudy ocean planets; $v = 7$ m/s

Fig. 18. Similar to Figs. 10b, 12b, and 14b for $f_c = 0.5$, but using a weighted sum of $\overline{\mathbf{F}}$ of a cloud-free ocean planet ($f_c = 0.0$) and $\overline{\mathbf{F}}$ of a completely cloudy ocean planet ($f_c = 1.0$), with weighting factors equal to 0.5.

6. Summary and conclusion

We have presented the computed spectra of the total flux $\overline{F}$, the (linearly) polarized flux $\overline{Q}$, and the degree of (linear) polarization P_s of starlight that is reflected by cloud-free and cloudy dry planets and ocean planets, from the ultraviolet (300 nm) to the infrared (2500 nm), at a 1 nm wavelength resolution and at planetary phase angles α ranging from $90°$ to $170°$. The atmospheres of our model planets are Earth-like and cloud-free, with patchy clouds, or fully cloudy. The clouds consist of spherical, liquid water droplets. The ocean is composed of a Fresnel reflecting, wind-ruffled surface, with sea foam and shadows of waves, and below that a seawater body bounded below by a black surface.

Our results show that at wavelengths outside absorption bands, the ocean glint strongly increases $\overline{F}$ and $|\overline{Q}|$ with increasing α from $90°$. The increase is caused by the increase of the local reflection angles on the ocean waves, and with that by the increase of Fresnel reflected light, yielding a brighter glint. The increase is more apparent toward longer wavelengths, where the scattering optical thickness of the gaseous atmosphere is small. This wavelength dependence of the glint's visibility results in an intersection of the $\overline{F}$ and $|\overline{Q}|$ spectra for different phase angles at visible wavelengths.

Our results show that the advantage of measuring $\overline{Q}$ instead of $\overline{F}$ when trying to detect an exo-ocean, is that only in the presence of Fresnel reflection, a significant polarized flux $|\overline{Q}|$ is expected at wavelengths larger than ~700 nm. According to Cowan et al. (2012), false positive ocean signatures could appear

a weighted sum approach to mimic an ocean planet with a cloud fraction f_c of 0.5. When comparing these curves with those in Figs. 10b, 12b, and 14b, which pertain to an actual horizontally inhomogeneous ocean planet with patchy clouds and the same $f_c = 0.5$ with a cloud-free glint, it is clear that the weighted sum planet has a weaker glint signature. Indeed, the weighted sum planet has a (polarized) flux due to the glint that is half of that of the horizontally inhomogeneous ocean planet with patchy clouds.
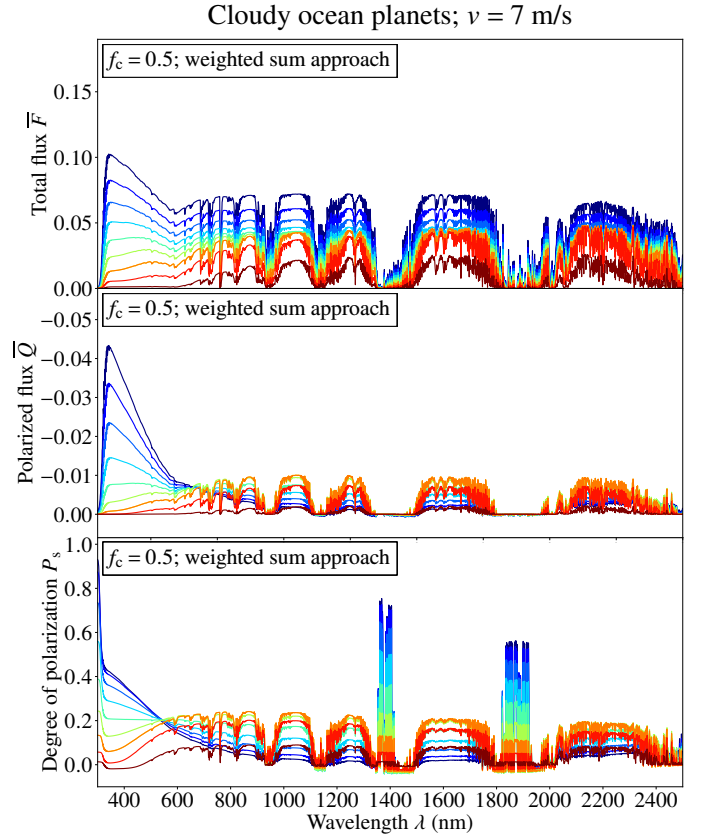
in $\overline{F}$ for planets with reflecting dry surfaces or polar caps. Our results indeed show that $\overline{F}$ can be nonzero and spectrally flat for dry planets with spectrally flat, bright surfaces and/or water clouds. Moreover, we find that in the near-infrared ($\lambda \gtrsim 700$ nm), a negative polarized flux $\overline{Q}$ (thus a direction of polarization that is perpendicular to the plane through the planet, the star, and the observer) only appears for an ocean planet with a visible glint. For all (cloudy and cloud-free) dry planets and for ocean planets that are completely covered by optically thick clouds, $\overline{Q}$ is near zero or slightly positive. A significant amount of negative $\overline{Q}$ in the near-infrared, at phase angles up from $90°$ appears to reveal the presence of an ocean.

In the spectra of the degree of polarization P_s, we find high values of P_s outside absorption bands for ocean planets where the glint is cloud-free. This ocean signature is increasingly apparent with increasing wavelength, thus with decreasing atmospheric gaseous optical thickness. The high P_s-values that result from the glint are caused by the shift of the maximum P_s from the single scattering Rayleigh peak near $\alpha = 90°$ to the Brewster angle at larger values of α, as explained by Zugger et al. (2010) and Trees & Stam (2019).

The glint can cause the continuum-P_s to be higher than the usually relatively high P_s-values from single Rayleigh scattering by gaseous molecules. Consequently, in gaseous absorption bands, where the glint signal from the ocean surface is absorbed by the gas, and where P_s attains its value for single Rayleigh scattering, the P_s spectrum will show dips in the bands. According to our computations, such dips only occur for ocean planets that are either cloud-free or that have patchy clouds that do not cover the glint. For dry planets, P_s shows either no structure or peaks in absorption bands.

We specifically investigated the dips of P_s in the H_2O absorption bands between $\lambda = 850$ and 1000 nm, and found that the depth and shape of the dips depend on the H_2O VMR, the cloud optical thickness (in case of a cloud-covered glint), the cloud altitude and the cloud coverage fraction (in case of a cloud-free glint). For all model planets, dips in the spectra of P_s were only observed when an ocean surface is present.

Furthermore, our results show that the blue color of the water body of an ocean could only be considered for ocean detection at wavelengths shorter than ~550 nm, where the ocean reflection slightly increases $\overline{F}$ and even more slightly $|\overline{Q}|$, which results in a shallow, broad dip in P_s. At longer wavelengths, the light that enters the ocean is increasingly absorbed by the water body. When clouds contribute to the reflected light signal, the color signature of the ocean's water virtually disappears.

The foam on the surface of our model oceans reflects incident light at all wavelengths between 300 and 2500 nm, although its albedo decreases with increasing wavelength. We only found a noticeable decrease of P_s due to the foam at the wind speed v of 13 m s^{-1} (which is considered to be a strong breeze on Earth), where the foam covers 2.46% of the ocean surface, and then at $\alpha = 90°$ and $100°$, as at those phase angles, the optical path through the atmosphere is shorter than for the larger values of α that we consider. Of course, although not explicitly studied here, for even higher wind speeds and smaller phase angles, the foam signature is expected to be stronger, and with clouds covering the ocean, the signature is expected to be weaker.

The signature of the glint in the total and polarized fluxes and in the degree of polarization is not directly limited by the cloud coverage fraction f_c, at it depends significantly on the horizontal cloud distribution: a cloud-free glint leaves clear signatures in the spectra, but if it is covered by a cloud patch, the signature

disappears. In case of a random patchy cloud cover, the probability of a cloud-free glint is higher when the wind speed is lower such that the glint is narrower (see Trees & Stam 2019, who generated 300 random patchy cloud patterns for each phase angle). The probability of a cloud-free glint of course decreases with increasing f_c, but a (partly) cloud-free glint at least part of the time is possible as long as there are gaps in the cloud deck. For future observations of Earth-like planets, multiple observations over time would increase the probability of catching a cloud-free glint, improving the odds of a successful ocean detection.

Trees & Stam (2019) already showed that a reddening of the degree of polarization and the polarized flux could reveal the presence of an ocean if consecutive measurements are taken at a range of phase angles. Between observations at different phase angles, the optical properties of a planet can change, for example when weather systems evolve. The polarimetric glint signatures in the spectra of this paper could reveal the presence of an ocean with a measurement at a single phase angle. Dips in P_s, and a negative $\overline{Q}$ in the near-infrared, can already be searched for at a planetary phase angle of $\alpha = 90°$, which would in principle be possible for any orbital inclination angle (see Stam 2008), and where the angular separation between the star and the planet is largest (which would be optimal for measuring the resolved planetary signal). This makes spectropolarimetry a strong tool for the detection of oceans on exoplanets, as the glint in the total flux, as measured when polarization is ignored, is only distinctive in the most crescent phases.

References

Aben, I., Helderman, F., Stam, D. M., & Stammes, P. 1999, Geophys. Res. Lett., 26, 591
Bates, D. R. 1984, Planet. Space Sci., 32, 785
Bazzon, A., Schmid, H. M., & Gisler, D. 2013, A&A, 556, A117
Berdyugina, S. V., Berdyugin, A. V., Fluri, D. M., & Piirola, V. 2011, ApJ, 728, L6
Bouret, J.-C., Neiner, C., Gómez de Castro, A. I., et al. 2018, Proc. SPIE Conf. Ser., 10699, 106993B
Chowdhary, J., Cairns, B., & Travis, L. D. 2006, Appl. Opt., 45, 5542
Chowdhary, J., Zhai, P.-W., Boss, E., et al. 2019, Front. Earth Sci., 7, 100
Chowdhary, J., Zhai, P.-W., Xu, F., Frouin, R., & Ramon, D. 2020, J. Quant. Spectr. Rad. Transf., 242, 106717
Cotton, D. V., Marshall, J. P., Bailey, J., et al. 2017, MNRAS, 467, 873
Cowan, N. B., Agol, E., Meadows, V. S., et al. 2009, ApJ, 700, 915
Cowan, N. B., Abbot, D. S., & Voigt, A. 2012, ApJ, 752, L3
Cox, C., & Munk, W. 1954, J. Opt. Soc. Am., 1917–1983, 838
de Haan, J. F., Bosma, P. B., & Hovenier, J. W. 1987, A&A, 183, 371
Deming, D., Wilkins, A., McCullough, P., et al. 2013, ApJ, 774, 95
De Rooij, W. A., & van der Stap, C. C. A. H. 1984, A&A, 131, 237
Emde, C., Buras-Schnell, R., Sterzik, M., & Bagnulo, S. 2017, A&A, 605, A2
Fraine, J., Deming, D., Benneke, B., et al. 2014, Nature, 513, 526
Fujii, Y., Turner, E. L., & Suto, Y. 2013, ApJ, 765, 76
Gordon, I., Rothman, L., Hill, C., et al. 2017, J. Quant. Spectr. Rad. Transf., 203, 3
Gorshelev, V., Serdyuchenko, A., Weber, M., Chehade, W., & Burrows, J. P. 2014, Atmos. Meas. Tech., 7, 609
Hale, G. M., & Querry, M. R. 1973, Appl. Opt., 12, 555
Hansen, J. E., & Travis, L. D. 1974, Space Sci. Rev., 16, 527
Hoeijmakers, H. J., Arts, M. L. J., Snik, F., et al. 2016, Opt. Exp., 24, 21435
Hovenier, J. W., & van der Mee, C. V. M. 1983, A&A, 128, 1
Hovenier, J. W., van der Mee, C., & Domke, H. 2004, Transfer of Polarized Light in Planetary Atmospheres; Basic Concepts and Practical Methods (Kluwer, Dordrecht: Springer)
Irwin, P. G. J., Teanby, N. A., de Kok, R., et al. 2008, J. Quant. Spectr. Rad. Transf., 109, 1136
Karalidi, T., Stam, D. M., Snik, F., et al. 2012, Planet. Space Sci., 74, 202
Kasper, M., Beuzit, J.-L., Verinaud, C., et al. 2010, SPIE Conf. Ser., 7735, 77352E
Kasting, J. F., Whitmire, D. P., & Reynolds, R. T. 1993, Icarus, 101, 108
Keller, C. U., Schmid, H. M., Venema, L. B., et al. 2010, SPIE Conf. Ser., 7735, 77356G

Kemp, J. C., Henson, G. D., Steiner, C. T., & Powell, E. R. 1987, Nature, 326, 270

Klindžić, D., Stam, D. M., Snik, F., et al. 2021, Philos. Trans. R. Soc. London Ser. A, 379, 20190577

Kochanov, R., Gordon, I., Rothman, L., et al. 2016, J. Quant. Spectr. Rad. Transf., 177, 15

Koepke, P. 1984, Appl. Opt., 23, 1816

Kopparapu, R. K., Wolf, E. T., & Meadows, V. S. 2020, in Planetary Astrobiology, eds. V. S. Meadows, G. N. Arney, B. E. Schmidt, & D. J. Des Marais (Tucson: The University of Arizona Press), 449

Kostogryz, N., Yakobchuk, T., & Berdyugina, S. 2015, ApJ, 806, 97

Kreidberg, L., Bean, J. L., Désert, J.-M., et al. 2014, ApJ, 793, L27

Kreidberg, L., Line, M. R., Bean, J. L., et al. 2015, ApJ, 814, 66

Lacis, A. A., & Oinas, V. 1991, J. Geophys. Res., 96, 9027

Line, M. R., Stevenson, K. B., Bean, J., et al. 2016, AJ, 152, 203

Livengood, T. A., Deming, L. D., A'Hearn, M. F., et al. 2011, Astrobiology, 11, 907

Lustig-Yaeger, J., Meadows, V. S., Tovar Mendoza, G., et al. 2018, ApJ, 156, 301

McClatchey, R., Fenn, R., Selby, J., Volz, F., & Garing, J. 1972, Optical Properties of the Atmosphere, AFCRL-72.0497 (USA: U.S. Air Force Cambridge Research Labs)

Miles-Páez, P. A., Pallé, E., & Zapatero Osorio, M. R. 2014, A&A, 562, L5

Mishchenko, M. I., & Travis, L. D. 1997, J. Geophys. Res., 102, 16989

Monahan, E. C., & Ó Muircheartaigh, I. 1980, J. Phys. Oceanograph., 10, 2094

Morel, A. 1974, Opt. Aspects Oceanograph., 1, 1

Nakajima, T. 1983, J. Quant. Spectr. Rad. Transf., 29, 521

Oakley, P. H. H., & Cash, W. 2009, ApJ, 700, 1428

Peck, E. R., & Reeder, K. 1972, J. Opt. Soc. Am., 62, 958

Pope, R. M., & Fry, E. S. 1997, Appl. Opt., 36, 8710

Robinson, T. D., Meadows, V. S., & Crisp, D. 2010, ApJ, 721, L67

Robinson, T. D., Ennico, K., Meadows, V. S., et al. 2014, ApJ, 787, 171

Rossi, L., Berzosa-Molina, J., & Stam, D. M. 2018, A&A, 616, A147

Ryan, D. J., & Robinson, T. D. 2022, Planet. Sci. J., 3, 33

Sancer, M. 1969, IEEE Trans. Antennas Propag., 17, 577

Seager, S., Whitney, B. A., & Sasselov, D. D. 2000, ApJ, 540, 504

Serdyuchenko, A., Gorshelev, V., Weber, M., Chehade, W., & Burrows, J. P. 2014, Atmos. Measur. Tech., 7, 625

Smith, B. 1967, IEEE Trans. Antennas Propag., 15, 668

Smith, R. C., & Baker, K. S. 1981, Appl. Opt., 20, 177

Sogandares, F. M., & Fry, E. S. 1997, Appl. Opt., 36, 8699

Stam, D. M. 2008, A&A, 482, 989

Stam, D. M., De Haan, J. F., Hovenier, J. W., & Stammes, P. 1999, J. Geophys. Res., 104, 16843

Stam, D. M., de Haan, J. F., Hovenier, J. W., & Stammes, P. 2000, J. Quant. Spectr. Rad. Transf., 64, 131

Stam, D. M., Hovenier, J. W., & Waters, L. B. F. M. 2004, A&A, 428, 663

Stam, D. M., de Rooij, W. A., Cornet, G., & Hovenier, J. W. 2006, A&A, 452, 669

Sterzik, M. F., Bagnulo, S., & Palle, E. 2012, Nature, 483, 64

Sterzik, M. F., Bagnulo, S., Stam, D. M., Emde, C., & Manev, M. 2019, A&A, 622, A41

Sterzik, M. F., Bagnulo, S., Emde, C., & Manev, M. 2020, A&A, 639, A89

Takahashi, J., Itoh, Y., Akitaya, H., et al. 2013, PASJ, 65, 38

Takahashi, J., Itoh, Y., Matsuo, T., et al. 2021, A&A, 653, A99

Tinetti, G., Vidal-Madjar, A., Liang, M.-C., et al. 2007, Nature, 448, 169

Trees, V. J. H., & Stam, D. M. 2019, A&A, 626, A129

Tsiaras, A., Waldmann, I. P., Tinetti, G., Tennyson, J., & Yurchenko, S. N. 2019, Nat. Astron., 3, 1086

Werdell, P. J., Behrenfeld, M. J., Bontempi, P. S., et al. 2019, Bull. Am. Meteor. Soc., 100, 1775

Williams, D. M., & Gaidos, E. 2008, Icarus, 195, 927

Zhai, P.-W., Hu, Y., Chowdhary, J., et al. 2010, J. Quant. Spectr. Rad. Transf., 111, 1025

Zugger, M. E., Kasting, J. F., Williams, D. M., Kane, T. J., & Philbrick, C. R. 2010, ApJ, 723, 1168

Zugger, M. E., Kasting, J. F., Williams, D. M., Kane, T. J., & Philbrick, C. R. 2011, ApJ, 739, 12